The Astrophysical Journal, 917:72 (22pp), 2021 August 20 https://doi.org/10.3847/1538-4357/ac0973

Estimating Dust Attenuation From Galactic Spectra. II. Stellar and Gas Attenuation in Star-forming and Diffuse Ionized Gas Regions in MaNGA

Niu Li[1], Cheng Li[1], Houjun Mo[2], Shuang Zhou[1], Fu-heng Liang[1], Médéric Boquien[3], Niv Drory[4], José G. Fernández-Trincado[5], Michael Greener[6], and Rogério Riffel[7,8]
[1] Department of Astronomy, Tsinghua University, Beijing 100084, People's Republic of China; liniu@tsinghua.edu.cn, cli2015@tsinghua.edu.cn
[2] Department of Astronomy, University of Massachusetts Amherst, MA 01003, USA
[3] Centro de Astronomía, Universidad de Antofagasta, Avenida Angamos 601, Antofagasta 1270300, Chile
[4] McDonald Observatory, University of Texas at Austin, 1 University Station, Austin, TX 78712, USA
[5] Instituto de Astronomía y Ciencias Planetarias, Universidad de Atacama, Copayapu 485, Copiapó, Chile
[6] School of Physics and Astronomy, University of Nottingham, University Park, Nottingham, NG7 2RD, UK
[7] Instituto de Física, Universidade Federal do Rio Grande do Sul, Campus do Vale, Porto Alegre, RS, 91501-970, Brazil
[8] Laboratório Interinstitucional de e-Astronomia—LIneA, Rua Gal. José Cristino 77, Rio de Janeiro, RJ—20921-400, Brazil
Received 2021 February 28; revised 2021 June 2; accepted 2021 June 7; published 2021 August 18

Abstract

We investigate the dust attenuation in both stellar populations and ionized gas in kiloparsec-scale regions in nearby galaxies using integral field spectroscopy data from MaNGA MPL-9. We identify star-forming (H II) and diffuse ionized gas (DIG) regions from MaNGA data cubes. From the stacked spectrum of each region, we measure the stellar attenuation, $E(B-V)_{\rm star}$, using the technique developed by Li et al., as well as the gas attenuation, $E(B-V)_{\rm gas}$, from the Balmer decrement. We then examine the correlation of $E(B-V)_{\rm star}$, $E(B-V)_{\rm gas}$, $E(B-V)_{\rm gas}-E(B-V)_{\rm star}$, and $E(B-V)_{\rm star}/E(B-V)_{\rm gas}$ with 16 regional/global properties, and for regions with different Hα surface brightnesses ($\Sigma_{\rm H\alpha}$). We find a stronger correlation between $E(B-V)_{\rm star}$ and $E(B-V)_{\rm gas}$ in regions of higher $\Sigma_{\rm H\alpha}$. The luminosity-weighted age (t_L) is found to be the property that is the most strongly correlated with $E(B-V)_{\rm star}$, and consequently, with $E(B-V)_{\rm gas}-E(B-V)_{\rm star}$ and $E(B-V)_{\rm star}/E(B-V)_{\rm gas}$. At fixed $\Sigma_{\rm H\alpha}$, $\log_{10}t_L$ is linearly and negatively correlated with $E(B-V)_{\rm star}/E(B-V)_{\rm gas}$ at all ages. Gas-phase metallicity and ionization level are important for the attenuation in the gas. Our results indicate that the ionizing source for DIG regions is likely distributed in the outskirts of galaxies, while for H II regions, our results can be well explained by the two-component dust model of Charlot & Fall.

Unified Astronomy Thesaurus concepts: Interstellar dust (836); Interstellar dust extinction (837); Stellar populations (1622); Hot ionized medium (752); Warm ionized medium (1788); Galaxy spectroscopy (2171); Emission nebulae (461); Interstellar extinction (841); Star formation (1569); Star forming regions (1565)

1. Introduction

Dust accounts for $\lesssim$1% of the interstellar medium (ISM) mass in a typical galaxy, but has an important influence on the spectral energy distribution (SED) of the galaxy through absorbing and scattering the starlight. This effect is known as dust attenuation or dust extinction (see reviews by Galliano et al. 2018; Salim & Narayanan 2020). Dust is produced from the ejecta of asymptotic giant branch (AGB) stars and supernovae (e.g., Dwek 1998; Nanni et al. 2013; Schneider et al. 2014; Aoyama et al. 2017; Popping et al. 2017), and it grows in the ISM by accreting gas-phase metals (e.g., Dominik & Tielens 1997; Dwek 1998; Hirashita & Kuo 2011; Zhukovska 2014). Dust can be destroyed by supernova shocks, thermal sputtering, and grain collisions, or it can be incorporated into newly born stars (e.g., Dwek 1998; Bianchi & Ferrara 2005; Nozawa et al. 2007). As dust attenuation can cause changes in the overall shape of galactic spectra and SEDs, one has to consider and correct for the effect of attenuation in order to reliably measure the intrinsic properties of galaxies from their observed spectra and SEDs.

A variety of methods have been used to estimate the stellar continuum dust attenuation, $E(B-V)_{\rm star}$. Dust extinction can be probed by observing individual stars along different lines of sight in the Milky Way or very nearby galaxies (e.g., Prevot et al. 1984; Cardelli et al. 1989; Fitzpatrick 1999; Gordon et al. 2003). Shorter-wavelength photons are more susceptible to dust attenuation, and dust can re-emit photons in the infrared. Thus, the $L_{\rm IR}/L_{\rm UV}$ ratio (known as IRX; e.g., Meurer et al. 1999; Gordon et al. 2000) is often used to estimate the dust attenuation. A galactic spectrum contains a variety of information about the physical properties of the galaxy. A simple approach to estimating dust attenuation through a galactic spectrum is to match the attenuated spectrum with the spectra of unattenuated galaxies that have similar stellar populations (e.g., Calzetti et al. 2000; Wild et al. 2011; Reddy et al. 2015; Battisti et al. 2017a, 2017b). Alternatively, fitting the SED (or full spectrum) with a stellar population synthesis model is also widely adopted to obtain the stellar attenuation (e.g., Cid Fernandes et al. 2005; Asari et al. 2007; Riffel et al. 2009, 2021; Conroy 2013; Wilkinson et al. 2015; Ge et al. 2018; Boquien et al. 2019; Li et al. 2020). In ionized gas regions, the dust attenuation on emission lines, $E(B-V)_{\rm gas}$, is commonly estimated from the Balmer decrement Hα/Hβ. The intrinsic line ratio can be calculated by atomic physics applied to a given environment (Osterbrock & Ferland 2006).

However, previous studies found that $E(B-V)_{\rm gas}$ is not consistent with $E(B-V)_{\rm star}$. Fanelli et al. (1988) found that $E(B-V)_{\rm gas}$ is significantly higher than $E(B-V)_{\rm star}$. Calzetti et al. (1994, 2000) further confirmed the result and found that the typical value of the ratio $f=E(B-V)_{\rm star}/E(B-V)_{\rm gas}$ is about 0.44. Moreover, studies based on both the local and high redshift galaxies show that $E(B-V)_{\rm gas}$ tends to be larger than $E(B-V)_{\rm star}$ (e.g., Wuyts et al. 2011, 2013; Kreckel et al. 2013; Price et al. 2014; Pannella et al. 2015; Zahid et al. 2017; Buat et al. 2018; Koyama et al. 2019), which is also seen in the near-infrared (e.g., Riffel et al. 2008). The value of f found in the literature varies over a wide range, from 0.44 to $\sim$1 (e.g., Calzetti et al. 1994; Reddy et al. 2010; Wuyts et al. 2011; Kashino et al. 2013; Price et al. 2014; Pannella et al. 2015; Valentino et al. 2015; Puglisi et al. 2016), and the variation is found to be correlated with the physical properties of galaxies, such as the total stellar mass (e.g., Zahid et al. 2017; Koyama et al. 2019), the specific star formation rate (sSFR; e.g., Wild et al. 2011; Price et al. 2014; Koyama et al. 2019; Qin et al. 2019), and the axial ratio (b/a; Wild et al. 2011).

In general, the discrepancy between the two attenuations may be explained by a two-component dust model (e.g., Charlot & Fall 2000; Wild et al. 2011; Chevallard et al. 2013), which includes an optically thin, diffuse component distributed throughout the ISM and an optically thick, dense component (the birth clouds) in which young stars are born. The typical lifetime of a birth cloud is about 10^7 yr (Blitz & Shu 1980; Charlot & Fall 2000). In this model, the emission lines are produced in the H II regions of the birth clouds, and stars younger than 3×10^6 yr produce most of the ionizing photons. Thus the emission lines and the continuum radiation of young stars in birth clouds are attenuated by both the dust in the ambient ISM and the dust in the birth clouds, while the continuum radiation of older stars is attenuated only by the diffuse dust in the ambient ISM (Charlot & Fall 2000). Consequently, emission lines are more strongly attenuated than the stellar continuum if the observed region is dominated by older stars. Only in idealized cases where one can resolve individual birth clouds or regions dominated by young stars in birth clouds are the two attenuations expected to be roughly the same (e.g., Basu-Zych et al. 2007).

However, previous studies of dust attenuation have been mostly based on global properties of galaxies. As dust attenuations depend on the geometrical distribution of the dust relative to stars (e.g., Charlot & Fall 2000; Wild et al. 2011), the relation between $E(B-V)_{\rm star}$ and $E(B-V)_{\rm gas}$ may be driven by local properties within galaxies. With the advent of new integral field unit (IFU) facilities, such as the Calar Alto Legacy Integral Field Area survey (CALIFA; Sánchez et al. 2012a), the Sydney Australian Astronomical Observatory Multi-object Integral Field Spectrograph survey (SAMI; Croom et al. 2012), the Multi Unit Spectroscopic Explorer Wide survey (MUSE-Wide; Urrutia et al. 2019), and the Mapping Nearby Galaxies at Apache Point Observatory survey (MaNGA; Bundy et al. 2015), spatially resolved spectroscopy can be used to provide large samples on which the properties of regions within individual galaxies can be studied. In addition, most previous studies focused on galaxies or regions that have a high star formation rate (SFR), ignoring the diffuse ionized gas (DIG; Haffner et al. 2009) regions. As the mechanisms of producing emission lines are quite different between DIG and H II regions (e.g., Zhang et al. 2017), the relation between $E(B-V)_{\rm star}$ and $E(B-V)_{\rm gas}$ may also be different between the two. Spatially resolved spectroscopy provides a way to divide a galaxy into DIG-dominated and H II-dominated regions, whereby it becomes possible to investigate dust attenuation in different types of regions (e.g., Tomičić et al. 2017; Zhang et al. 2017; Lacerda et al. 2018).

Recently, using data of MaNGA galaxies in the Sloan Digital Sky Survey Data Release 15 (SDSS DR15; Aguado et al. 2019) and MaNGA value-added catalog (VAC) of the `Pipe3D` pipeline (Sánchez et al. 2018), Lin & Kong (2020) investigated the variations of f from subgalactic to galactic scales. They found that $E(B-V)_{\rm star}$ and $E(B-V)_{\rm gas}$ have a stronger correlation for more active H II regions, while f is found to have a moderate correlation with tracers of DIG regions. Their results suggest that local physical conditions, such as metallicity and ionization level, play an important role in determining f, in that metal-poor regions with a higher ionized level have larger f. Using a sample of 232 star-forming spiral galaxies from MaNGA and the full spectral fitting code `STARLIGHT` (Cid Fernandes et al. 2005), Greener et al. (2020) also found that the variation in dust attenuation properties is likely driven by local physical properties of galaxies, such as the SFR surface density. Riffel et al. (2021) analyzed a sample of 170 active galactic nucleus (AGN) hosts with strong star formation and a control sample of 291 star-forming galaxies from MaNGA. They also found a strong correlation between $E(B-V)_{\rm star}$ (derived with `STARLIGHT`) and $E(B-V)_{\rm gas}$, with $f\sim0.37$, which is close to but slightly lower than the typical value of $f=0.44$ found for the general population of star-forming regions.

In this paper, we use the latest internal data release of MaNGA, the MaNGA Product Launch 9 (MPL-9), of about 8000 unique galaxies (4621 in SDSS DR15) to explore the correlation between $E(B-V)_{\rm star}$ and $E(B-V)_{\rm gas}$ in DIG and H II regions to study how f correlates with physical properties of galaxies and whether the two-component model works on spatially resolved regions. Our analysis improves upon earlier analyses by using a much larger sample and by adopting a new method for estimating the dust attenuation from full optical spectral fitting (Li et al. 2020, hereafter Paper I). In addition, following the Wolf–Rayet search procedure of Liang et al. (2020), we perform spatial binning for each data cube according to the $\Sigma_{\rm H\alpha}$ map instead of the continuum signal-to-noise ratio (S/N) map. The ionized gas regions identified in this way are expected to be more uniform and smoother in terms of physical properties than those binned by S/N.

This paper is organized as follows. Section 2 describes the observational data, quantities measured from the data, and the samples for our analysis. In Section 3 we present our main results. We discuss and compare our results with those obtained previously in Section 4. Finally, we summarize our results in Section 5. Throughout this paper we assume a Λ cold dark matter cosmology model with $\Omega_{\rm m}=0.3$, $\Omega_\Lambda=0.7$, and $H_0=70\,{\rm km\,s^{-1}\,Mpc^{-1}}$, and a Chabrier (2003) initial mass function (IMF).

2. Data

2.1. Overview of MaNGA

The MaNGA survey is one of the three core programs of the fourth-generation Sloan Digital Sky Survey project (SDSS-IV; Blanton et al. 2017). During the past six years from 2014 July

through 2020 August, MaNGA has obtained integral field spectroscopy (IFS) for 10,010 nearby galaxies (Bundy et al. 2015). A total of 29 IFUs with various sizes are used to obtain the IFS data, including 17 science fiber bundles with five different fields of view (FoVs) ranging from 12″ (19 fibers) to 32″ (127 fibers), and 12 seven-fiber mini-bundles for flux calibration. Obtained with the two dual-channel BOSS spectrographs at the 2.5 m Sloan telescope (Gunn et al. 2006; Smee et al. 2013) and a typical exposure time of three hours, the MaNGA spectra cover a wavelength range from 3622 to 10354 Å with a spectral resolution of $R \sim 2000$, and they reach a target r-band S/N of 4–8 (Å^{-1} per 2″ fiber) at 1–2 effective radii (R_e) of galaxies. A detailed description of the MaNGA instrumentation can be found in Drory et al. (2015).

Targets of the MaNGA survey are selected from the NASA Sloan Atlas (NSA),[9] a catalog of ∼640,000 low-redshift galaxies constructed by Blanton et al. (2011) based on the SDSS, GALEX, and 2MASS. As detailed in Wake et al. (2017), the MaNGA sample selection is designed so as to simultaneously optimize the IFU size distribution, the IFU allocation strategy, and the number density of targets. The Primary and Secondary samples, which are the main samples of the survey, are selected to effectively have a flat distribution of the K-corrected i-band absolute magnitude (M_i), covering out to 1.5 and $2.5R_e$, respectively. In addition, the color-enhanced sample selects galaxies that are not well sampled by the main samples in the ner-UV (NUV) − r versus M_i diagram. Overall the MaNGA targets cover a wide range of stellar mass, $10^9 M_\odot \lesssim M_* \lesssim 6 \times 10^{11} M_\odot$, and a redshift range of $0.01 < z < 0.15$, with a median redshift of $z \sim 0.03$.

MaNGA raw data are reduced using the Data Reduction Pipeline (DRP; Law et al. 2016) and provide a data cube for each galaxy with a spaxel size of 0.″5 × 0.″5 with an effective spatial resolution that can be described by a Gaussian with a full width at half maximum (FWHM) of ∼2.″5. For more than 80% of the wavelength range, the absolute flux calibration of the MaNGA spectra is better than 5%. Details of the flux calibration, survey strategy and data quality tests are provided in Yan et al. (2016a, 2016b). In addition, MaNGA also provides products of the Data Analysis Pipeline (DAP; Westfall et al. 2019) developed by the MaNGA collaboration, which performs full spectral fitting to the DRP data cubes and obtains measurements of stellar kinematics, emission lines, and spectral indices. The latest data release from the MaNGA was made in SDSS DR15 (Aguado et al. 2019), including DRP and DAP products of 4824 data cubes for 4621 unique galaxies. In this paper, we make use of the latest internal sample, the MPL-9, which contains 8113 data cubes for 8000 unique galaxies.

2.2. Identifying Ionized Gas Regions

Our study aims to examine the spatially resolved dust attenuation in both starlight and ionized gas. To this end, we first identify ionized gas regions in the MaNGA galaxies and then measure the stellar and gas attenuation as well as other properties for each region. We make use of the Hα flux maps obtained by MaNGA DAP for the identification of ionized gas regions. Given the Hα flux map of a galaxy, we calculate the surface density of Hα emission $\Sigma_{\rm H\alpha}$ in units of $\text{erg s}^{-1}\,\text{kpc}^{-2}$ for each spaxel in the map and select all the spaxels with $\Sigma_{\rm H\alpha}$ exceeding a threshold of $\Sigma_{\rm H\alpha,min}$ for the identification. We have corrected the effect of dust attenuation on the Hα fluxes using the observed Balmer decrement, i.e., the Hα-to-Hβ flux ratio $(\rm H\alpha/H\beta)_{obs}$ with the Hβ flux also from the DAP, assuming case-B recombination with an intrinsic Balmer decrement $(\rm H\alpha/H\beta)_{int} = 2.86$ (Osterbrock & Ferland 2006).

We apply the public pipeline HIIEXPLORER[10] developed by Sánchez et al. (2012b) to the $\Sigma_{\rm H\alpha}$ map to identify ionized gas regions. The HIIEXPLORER begins by picking up the peak spaxel in the map, i.e., the one with the highest $\Sigma_{\rm H\alpha}$, as the center of an ionized gas region. The spaxels in the vicinity are then appended to the region if their distance from the center is less than $r_p^{\rm max}$ and if their $\Sigma_{\rm H\alpha}$ is higher than 10% of the central $\Sigma_{\rm H\alpha}$. The latter requirement aims to make the region roughly coherent. The region is then removed from the map, and the pipeline moves on to the peak spaxel of the remaining map. This process is repeated until every spaxel with $\Sigma_{\rm H\alpha} > \Sigma_{\rm H\alpha,min}$ is assigned to a region.

The HIIEXPLORER was initially designed for identifying H II regions, and so the threshold density $\Sigma_{\rm H\alpha,min}$ is usually set to be a relatively high value, e.g., $\Sigma_{\rm H\alpha,min} = 10^{39.5}\,\text{erg s}^{-1}\,\text{kpc}^{-2}$ in a recent MaNGA-based study by Liang et al. (2020). Here we adopt a much lower threshold, $\Sigma_{\rm H\alpha,min} = 10^{37.5}\,\text{erg s}^{-1}\,\text{kpc}^{-2}$, in order to extend to DIG regions. Following Liang et al. (2020), we set $r_p^{\rm max} = 1.''5$, which is comparable to but slightly higher than half of the MaNGA spatial resolution (2.″5, corresponding to ∼1.5 kpc at the MaNGA median redshift $z = 0.03$). Due to the limited resolution, one cannot resolve individual H II regions, whose sizes typically range from a few to hundreds of parsecs (e.g., Kennicutt 1984; Kim & Koo 2001; Hunt & Hirashita 2009; Lopez et al. 2011; Anderson et al. 2019). Therefore the ionized gas regions identified from MaNGA may contain a few to hundreds of individual H II regions, or be a mixture of DIG and H II regions. According to Zhang et al. (2017), $\Sigma_{\rm H\alpha}$ can be used to effectively separate DIG-dominated regions from H II-dominated regions in the MaNGA galaxies, with an empirical dividing value of $\sim 10^{39}\,\text{erg s}^{-1}\,\text{kpc}^{-2}$. In what follows, we refer to H II-dominated regions as H II regions and to DIG-dominated regions as DIG regions for simplicity.

The above process results in a total of $\sim 5 \times 10^5$ ionized gas regions down to $\Sigma_{\rm H\alpha,min} = 10^{37.5}\,\text{erg s}^{-1}\,\text{kpc}^{-2}$, out of 8000 galaxies from the MPL-9.

2.3. Measuring Stellar Attenuation

In our sample each ionized gas region contains a few to tens of spaxels that have similar $\Sigma_{\rm H\alpha}$ by definition. We stack the spectra within each region to obtain an average spectrum with high S/N, from which we then measure the stellar and gas attenuation, as well as other properties necessary for this work. We adopt the weighted mean estimator for the spectral stacking, which is described in detail in Liang et al. (2020). Briefly, the spectra in a given region are corrected to the rest-frame considering both the redshift of the host galaxy and the relative velocities of each spaxel, using the stellar velocity map from DAP, and the fluxes at each wavelength point are weighted by their spectral error provided by the MaNGA DRP. The error of the stacked spectrum is derived so as to correct for the effect of covariance by following the formula given in Figure 16 of Law et al. (2016). We find that the stacking process effectively reduces the noise in the original spectra: the S/N of the stacked spectra is higher than that of the original

[9] http://www.nsatlas.org

[10] http://www.caha.es/sanchez/HII_explorer/

spectra by ∼20% on average, ranging from about 15% at the highest S/N up to 50% at the lowest S/N. On average, one region contains ∼10 spaxels, and the typical final S/N is ∼12.

For each region we then estimate the relative attenuation curve ($A_\lambda - A_V$) and the stellar color excess $E(B-V)_{\rm star}$ by applying the method developed in Paper I to the stacked spectrum. In this method, the small-scale features (S) in the observed spectrum are first separated from the large-scale spectral shape (L) using a moving-average filter. The same separation is also performed for the spectrum of the model templates, and the intrinsic dust-free model spectrum of the stellar component is then derived by fitting the observed ratio of the small- to large-scale spectral components $(S/L)_{\rm obs}$ with the same ratio as for the model spectra $(S/L)_{\rm model}$. As shown in Paper I (see Section 2.1 and Equations (3)–(8) in that paper), the small- and large-scale components are attenuated by dust in the same way, so that their ratio S/L is dust free as long as the dust attenuation curves are similar for different stellar populations in a galactic region. Finally, $A_\lambda - A_V$ is derived by comparing the observed spectrum with the best-fit model spectrum. The value of $E(B-V)_{\rm star}$ $(=A_B - A_V)$ is then directly calculated from $A_\lambda - A_V$.

As shown in Paper I, one important advantage of this method is that the relative dust attenuation curve can be directly obtained without the need of assuming a functional form for the curve. Furthermore, extensive tests on mock spectra have shown that the method is able to recover the input dust attenuation curve accurately from an observed spectrum with S/N > 5 as long as the underlying stellar populations have similar dust attenuation or the optical depths are lower than unity. This method should be well valid in the current study, where the ionized gas regions are selected to each span a limited range of $\Sigma_{\rm H\alpha}$. They are therefore expected to have limited variations in the underlying stellar population properties.

2.4. Measuring Stellar Populations

Using the measurements of the relative dust attenuation curves obtained above, we correct the effect of dust attenuation for the stacked spectra of the ionized gas regions in our sample. We then perform full spectral fitting to the dust-free spectrum and measure both stellar population parameters from the best-fit stellar component and emission line parameters from the starlight-subtracted component. We use the simple stellar populations (SSPs) given by Bruzual & Charlot (2003, BC03) to fit our spectra. BC03 provides the spectra for a set of 1326 SSPs at a spectral resolution of 3 Å, covering 221 ages from $t = 0$ Gyr to $t = 20$ Gyr and six metallicities from $Z = 0.005 Z_\odot$ to $Z = 2.5 Z_\odot$, where the solar metallicity is $Z_\odot = 0.02$. The SSPs are computed using the Padova evolutionary track (Bertelli et al. 1994) and the Chabrier (2003) IMF. We select a subset of 150 SSPs that cover 25 ages at each of the six metallicities, ranging from $t = 0.001$ Gyr to $t = 13$ Gyr with approximately equal intervals in $\log_{10} t$. For a given region, we fit its spectrum $F(\lambda)$ with a linear combination of the SSPs,

$$F(\lambda) = \sum_{j=1}^{j=N_*} x_j f_{\rm SSP}^j(\lambda), \quad (1)$$

where $N_* = 150$, $f_{\rm SSP}^j(\lambda)$ is the spectrum of the jth SSP, and x_j is the coefficient of the jth SSP to be determined by the fitting. The effect of the stellar velocity dispersion is taken into account by convolving the SSPs in Equation (1) with a Gaussian. We have carefully masked out all the detected emission lines in the spectra following the scheme described in Li et al. (2005).

We then obtain the following parameters to quantify the stellar populations in each region based on the coefficients x_j of the best-fit stellar spectrum or the best-fit spectrum itself.

1. $\log_{10}\Sigma_*$—logarithm of the surface density of stellar mass given by $\Sigma_* = (\sum_{j=1}^{N_*} x_j M_j)/A$ in units of $M_\odot\,{\rm kpc}^{-2}$, where M_j is the stellar mass of the jth SSP and A is the area of the region.
2. $\log_{10} t_L$—logarithm of the light-weighted stellar age, given by $\log_{10} t_L = \sum_{j=1}^{N_*} x_j \log_{10} t_j$, where t_j is the age of the jth SSP in units of yr.
3. Z_L—light-weighted stellar metallicity, given by $Z_L = \sum_{j=1}^{N_*} x_j Z_j$, where Z_j is the metallicity of the jth SSP in units of solar metallicity.
4. $\log_{10} t_M$—logarithm of the mass-weighted stellar age, given by $\log_{10} t_M = (\sum_{j=1}^{N_*} x_j M_j \log_{10} t_j)\big/(\sum_{j=1}^{N_*} x_j M_j)$.
5. Z_M—mass-weighted stellar metallicity, given by $Z_M = (\sum_{j=1}^{N_*} x_j M_j Z_j)\big/(\sum_{j=1}^{N_*} x_j M_j)$.
6. D_n4000—the narrow-band version of the 4000 Å break, defined by Balogh et al. (1999). We measure this parameter from the best-fit stellar spectrum rather than the observed spectrum in order to minimize the effect of noise.

Because the spectra are corrected for dust attenuation before they are used for the spectral fitting, the known degeneracy between dust attenuation and stellar populations should be largely alleviated. This provides more reliable estimates of the stellar age and metallicity, as shown in Paper I (Appendix B), where extensive tests are made on mock spectra that cover wide ranges in age and metallicity and include realistic star formation histories and emission lines. In these tests, Bayesian inferences of the stellar age and metallicity are derived by applying the spectral fitting code `BIGS` (Zhou et al. 2019) to the mock spectra with the same set of BC03 SSPs as used here, with or without correcting the effect of dust attenuation before the fitting. It is found that the inference uncertainties for both stellar parameters are significantly reduced if the dust attenuation is corrected before the fitting (see their Figure B1 and B2).

2.5. Measuring Emission Lines and Gas Attenuations

We measure the flux, surface density, and equivalent width (EW) for a number of emission lines for each region, including [O II] λλ3726,3729, Hβ, [O III] λλ4959,5007, [N II] λλ6548, 6583, Hα, and [S II] λλ6717,6731. We subtract the best-fit stellar spectrum from the stacked spectrum, and fit the emission lines with Gaussian profiles. We use a single Gaussian to fit Hβ, [O III] λ4959, [O III] λ5007, [N II] λ6548, Hα, [N II] λ6583, [S II] λ6717 and [S II] λ6731, and a double Gaussian to fit [O II] λλ3726,3729. The line ratios of [N II] λ6583/[N II] λ6548 and [O III] λ5007/[O III] λ4959 are fixed to 3 during the fitting. The parameters of each line are then calculated from the Gaussian profiles, together with the best-fit stellar spectrum when needed. We have corrected the fluxes for the effect of

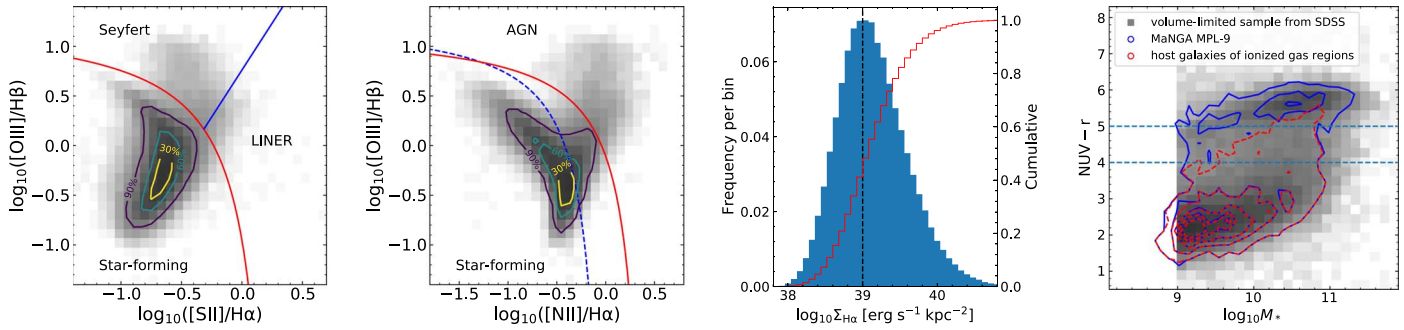

Figure 1. Panel (a1): the BPT diagram of the ionized gas regions identified from the MaNGA MPL-9. The red line from Kewley et al. (2001) and the blue line from Kewley et al. (2006) jointly divide the regions into three classes: star-forming regions (below the red line), Seyferts (above the two lines), and LINERs (above the red but below the blue line). The gray scale indicates the number density of the ionized gas regions in logarithm. The contours indicate the areas enclosing 30%, 60%, and 90% of the total sample. Panel (a2): similar to panel (a1), but for [O III] λ5007/Hβ vs. [N II] λ6583/Hα diagram. The red line is from Kewley et al. (2001) and the blue line is from Kauffmann et al. (2003a). Regions above the red line are classified as AGN. Panel (b): the histogram shows the distribution of dust-corrected $\Sigma_{\rm H\alpha}$ for the final sample of ionized gas regions. The red line shows the cumulative distribution of the final sample. Panel (c): diagram of NUV $-$ r color vs. stellar mass. The dashed red contours show the distribution of the galaxies hosting the ionized gas regions in our final sample. The blue contours show the distribution of the parent MaNGA MPL-9 sample. The gray-scale distribution in the background is for a volume-limited sample of galaxies selected from the SDSS with $M_* > 10^9 M_\odot$ and $0.01 < z < 0.03$. See the text in Section 2.6.

attenuation using the observed Hα-to-Hβ flux ratio as described in Section 2.2. For this, we have assumed case-B recombination. An estimate of the dust attenuation in the gas, as quantified by $E(B-V)_{\rm gas}$, is obtained for each region,

$$E(B-V)_{\rm gas} = \frac{2.5}{k(\lambda_{\rm H\beta}) - k(\lambda_{\rm H\alpha})} \log_{10}\left[\frac{({\rm H\alpha}/{\rm H\beta})_{\rm obs}}{2.86}\right], \quad (2)$$

where $k(\lambda_{\rm H\beta})$ and $k(\lambda_{\rm H\alpha})$ are the attenuation curves evaluated at the wavelength of Hα and Hβ. For each region, we use its attenuation curve measured from our method, as described in Section 2.3.

Based on the emission line measurements, we have estimated the following parameters to quantify gas-related properties.

1. $\log_{10}\Sigma_{\rm H\alpha}$—logarithm of the surface density of the Hα emission in units of erg s^{-1} kpc^{-2}.
2. $\log_{10}{\rm EW}_{\rm H\alpha}$—logarithm of the equivalent width of the Hα emission line in units of Å.
3. sSFR—specific SFR defined by the ratio of SFR to stellar mass in a region. The SFR is computed from the dust-corrected Hα luminosity following Kennicutt (1998), with a Chabrier (2003) IMF: ${\rm SFR}(M_\odot\,{\rm yr}^{-1}) = 4.6 \times 10^{-42} L_{\rm H\alpha}({\rm erg\,s^{-1}})$. The stellar mass is obtained above from the spectral fitting (Section 2.4).
4. 12+$\log_{10}$(O/H)—gas-phase metallicity. We adopt the O3N2 estimator in which the metallicity is empirically estimated from the parameter O3N2 $\equiv$ ([O III] λ5007/Hβ)/([N II] λ6583/Hα) (e.g., Alloin et al. 1979; Zaritsky et al. 1994; Pilyugin 2001; Denicoló et al. 2002; Pettini & Pagel 2004; Pilyugin & Thuan 2005).
5. $\log_{10}$([N II]/[O II])—logarithm of the flux ratio of [N II] λ6583 and [O II] $\lambda\lambda$3726,3729.
6. $\log_{10}$([O III]/[O II])— logarithm of the flux ratio of [O III] λ5007 and [O II] $\lambda\lambda$3726,3729.
7. $\log_{10}$([N II]/[S II])—logarithm of the flux ratio of [N II] λ6583 and [S II] λ6717.

2.6. Selection of Ionized Gas Regions

For our analysis we further select a subset of the ionized gas regions with substantially higher S/N in both the stellar continuum and the relevant emission lines. Specifically, we require S/N > 5 for the stellar continuum and the Hα and Hβ lines, and S/N > 3 for the [O II] $\lambda\lambda$3726,3729, [O III] λ5007, [N II] λ6583, and [S II] $\lambda\lambda$6717,6731. Furthermore, we exclude regions classified as AGN on the Baldwin–Phillips–Terlevich diagram (BPT; Baldwin et al. 1981). Figure 1 (panels (a1) and (a2)) displays the distribution of all the ionized gas regions in the planes of [O III]/Hβ versus [S II]/Hα and [O III]/Hβ versus [N II]/Hα. The majority of the regions are located in the area classified as star forming (or H II). We first exclude all the regions that are classified as Seyferts in the [O III]/Hβ versus [S II]/Hα diagram. We also exclude the regions that are located within 3″ from their galactic center and are classified as either LINER in the [O III]/Hβ versus [S II]/Hα diagram or as AGN in the [O III]/Hβ versus [N II]/Hα diagram.

These restrictions exclude about 45% of the ionized gas regions identified in Section 2.2, which results in a final sample of $\sim 2.7 \times 10^5$ regions. Panel (b) of Figure 1 displays the histogram of $\Sigma_{\rm H\alpha}$ of the final sample. The distribution is peaked at around 10^{39}erg s^{-1} kpc^{-2}, as indicated by the vertical dashed line. As mentioned above, $\Sigma_{\rm H\alpha} \sim 10^{39}$ erg s^{-1} kpc^{-2} can be used to effectively separate the low-$\Sigma_{\rm H\alpha}$ DIG regions from the high-$\Sigma_{\rm H\alpha}$ H II regions. Thus, about 40% of our sample are DIG regions, while 60% are H II regions. Panel (c) of Figure 1 displays the distribution of the galaxies that host our ionized gas regions in the NUV $-$ r versus $\log_{10} M_*$ plane, using data from the NSA (Blanton et al. 2011). For comparison, the distribution of the full sample of MaNGA MPL-9 is plotted as blue contours. We have also selected from the NSA a volume-limited sample consisting of $\sim 3.5 \times 10^4$ galaxies with stellar mass $M_* > 10^9 M_\odot$ and with redshift in the range $0.01 < z < 0.03$. The distribution of this sample is plotted as the gray background in the figure. Overall, galaxies in the MaNGA MPL-9 follow the general population. The host galaxies of our ionized gas regions are mostly found as the blue-cloud population (NUV–$r < 4$), with a considerable

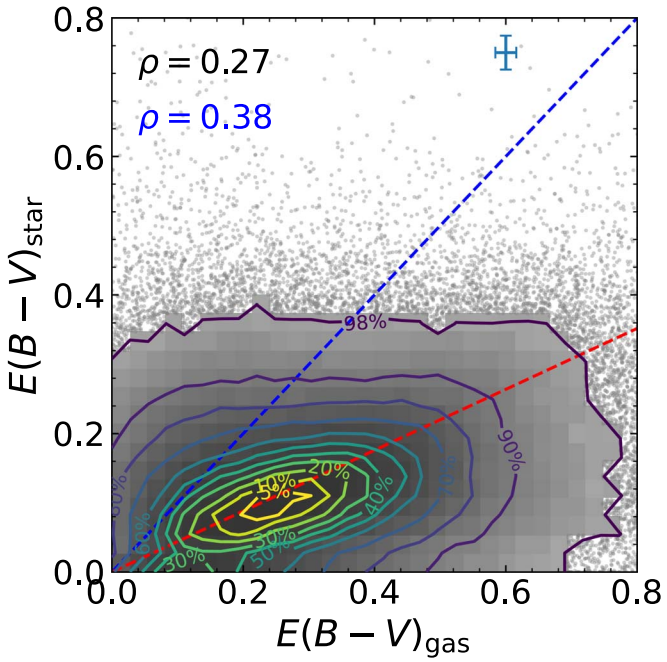

Figure 2. Distribution of the ionized gas regions in MaNGA galaxies in the diagram of $E(B-V)_{\rm star}$ vs. $E(B-V)_{\rm gas}$. Contours of the sample fraction are plotted, and the contour levels are indicated. Individual ionized gas regions are plotted as small dots outside the 98% area. The Spearman rank correlation coefficients (ρ) are indicated for both the full sample (black) and the H II regions (blue) selected by $\log_{10}\Sigma_{\rm H\alpha} > 39$. The dashed blue line indicates the 1:1 relation, while the dashed red line represents $E(B-V)_{\rm star} = 0.44\,E(B-V)_{\rm gas}$, which is the average relation of star-forming galaxies found by Calzetti et al. (2000). The typical uncertainties are shown in the upper right corner.

fraction at $M_* \gtrsim 10^{10} M_\odot$ extending to the green valley with $4 < {\rm NUV} < 5$, and with a small fraction at the highest mass end($M_* \sim 10^{11} M_\odot$) to the red sequence (NUV–$r > 5$).

3. Results

3.1. Correlations of Dust Attenuation with Regional/Global Properties of Galaxies

Figure 2 displays the distribution of all the ionized gas regions in our sample in the $E(B-V)_{\rm star}$ versus $E(B-V)_{\rm gas}$ plane. Overall, $E(B-V)_{\rm gas}$ spans a wider range than $E(B-V)_{\rm star}$, and there is a weak correlation between the two parameters. The Spearman rank correlation coefficients for both the full sample of ionized gas regions ($\rho = 0.27$) and the subset of H II regions of $\log_{10}\Sigma_{\rm H\alpha} > 39$ ($\rho = 0.38$) are quite low. For reference, we also plot the contours of the constant sample fraction at levels ranging from 5% to 98%, as well as two linear relations: the 1:1 relation (dashed blue line) and $E(B-V)_{\rm star} = 0.44\,E(B-V)_{\rm gas}$ (dashed red line), the previously found average relation of UV-bright starburst galaxies (e.g., Calzetti et al. 1994, 2000). The majority of the ionized gas regions lie slightly below the red line, with large scatter. More interestingly, a significant population of the ionized gas regions is located above the 1:1 line, where the stellar attenuation is stronger than the gas attenuation. A key goal of our study is to understand what drives the scatter in this diagram, in particular, the bimodal distribution divided (roughly) by the 1:1 line.

We examine the dependence of $E(B-V)_{\rm star}$, $E(B-V)_{\rm gas}$, $E(B-V)_{\rm gas} - E(B-V)_{\rm star}$, and $E(B-V)_{\rm star}/E(B-V)_{\rm gas}$ on a variety of physical properties, both regional and global, in order to find the driving factor(s) for the overall distribution shown in Figure 2. We consider 13 regional properties: $\log_{10}\Sigma_{\rm H\alpha}$, $\log_{10}{\rm EW}_{\rm H\alpha}$, sSFR, $\log_{10}\Sigma_*$, $\log_{10}t_L$, $\log_{10}t_M$, Z_L, Z_M, D_n4000, $12+\log_{10}({\rm O/H})$, $\log_{10}$[N II]/[O II], $\log_{10}$[O III]/[O II], and $\log_{10}$[N II]/[S II], which are described in Sections 2.4 and 2.5. In addition, three global properties are considered: total stellar mass (M_*), morphological type (T-type), and the r-band minor-to-major axial ratio (b/a). The measurements of M_* and b/a are taken from the NSA catalog (Blanton et al. 2005), and the estimates for the T-type come from Domínguez Sánchez et al. (2018). A negative T-type usually indicates an early-type morphology, while a positive T-type indicates a late type.

We find that out of the 16 regional/global properties, dust attenuation shows the strongest correlation with the following three: t_L for the stellar attenuation, and $\Sigma_{\rm H\alpha}$ and [N II]/[S II] for the gas attenuation. Figure 3 shows the distribution of the ionized gas regions in the $E(B-V)_{\rm star}$ versus $E(B-V)_{\rm gas}$ space, color-coded by the three properties (panels in the leftmost column), as well as the correlation of the four dust attenuation parameters ($E(B-V)_{\rm star}$, $E(B-V)_{\rm gas}$, and their difference and ratio) with the three properties (panels in Columns 2 to 5). In each of the correlation panels, the median relation and the 1σ scatter around the median relation are plotted as solid cyan lines for all the ionized gas regions in our sample and as dashed blue lines for the subset of H II regions of $\log_{10}\Sigma_{\rm H\alpha} > 39$. The Spearman rank correlation coefficients (ρ) are indicated for both the full sample and the subset. Results for the rest 13 properties, plotted in the same way, are presented in Appendix A.

By comparing the Spearman rank correlation coefficients, one can see that the stellar attenuation parameter $E(B-V)_{\rm star}$ shows the strongest (negative) correlation with stellar age. For the full sample, $\rho = -0.569$ for the luminosity-weighted age ($\log_{10}t_L$) and $\rho = -0.627$ for the mass-weighted age ($\log_{10}t_M$; see Appendix A). The stellar attenuation decreases with increasing t_L, from an average of $E(B-V)_{\rm star} \sim 0.3$ at $\log_{10}(t_L/{\rm yr}) \sim 7.5$ down to about zero at the oldest age, as can be seen from the first row of Figure 3. The correlation of $E(B-V)_{\rm star}$ with the other 12 properties is much weaker, with $|\rho| < 0.2$ for all properties except for the sSFR, for which $\rho = 0.339$. Similar results are obtained when the analysis is limited to H II regions. These results strongly suggest that the stellar age is the dominant parameter in driving the stellar attenuation for both H II and DIG regions. Compared to the mass-weighted stellar age ($\log_{10}t_M$), the luminosity-weighted age ($\log_{10}t_L$) shows a more linear correlation with stellar attenuation, although with a slightly smaller correlation coefficient. In addition, from the first row of Figure 3, one can see that the stellar age is positively correlated with the gas attenuation, although with a relatively small correlation coefficient ($\rho = 0.183$). Consequently, $E(B-V)_{\rm gas} - E(B-V)_{\rm star}$ increases with t_L, while $E(B-V)_{\rm star}/E(B-V)_{\rm gas}$ decreases. Of all the properties and all the attenuation parameters, the strongest correlation is found between $E(B-V)_{\rm star}/E(B-V)_{\rm gas}$ and $\log_{10}t_L$, with $\rho = -0.631$. Thus, the driving role of $\log_{10}t_L$ in $E(B-V)_{\rm gas} - E(B-V)_{\rm star}$ and $E(B-V)_{\rm star}/E(B-V)_{\rm gas}$ comes mainly from the strong correlation between $E(B-V)_{\rm star}$ and $\log_{10}t_L$, and the correlations of $E(B-V)_{\rm gas} - E(B-V)_{\rm star}$ and $E(B-V)_{\rm star}/E(B-V)_{\rm gas}$ with other properties are largely produced by this strong correlation with age.

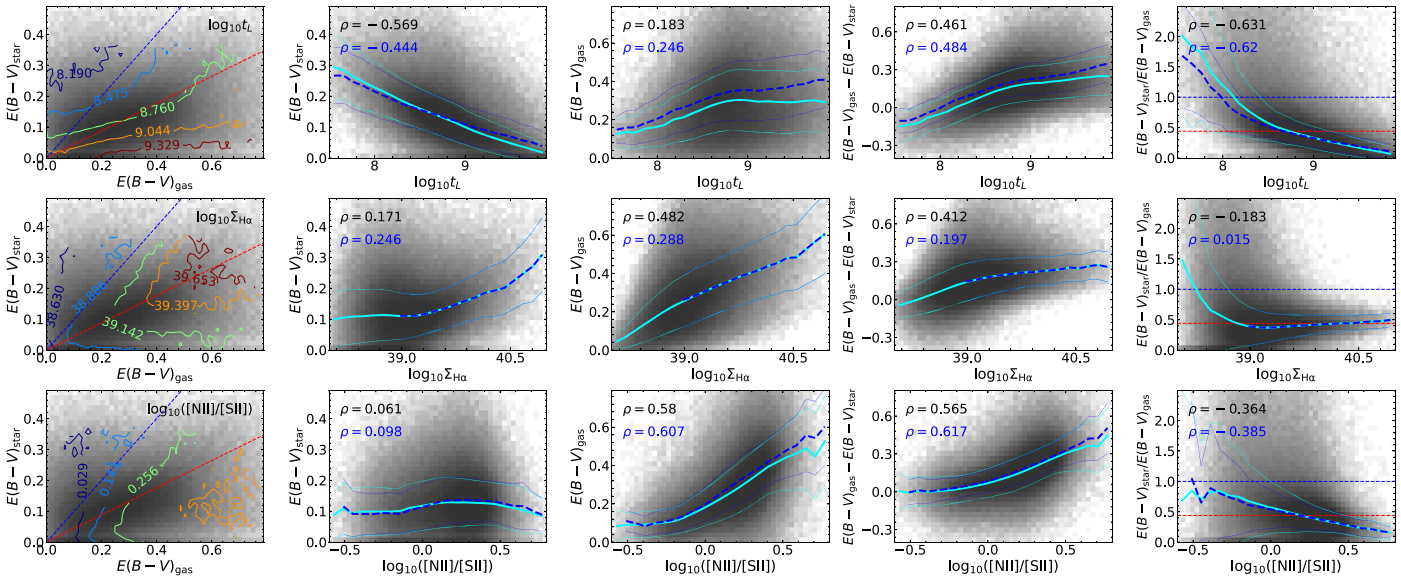

Figure 3. Correlations of $E(B-V)_{\rm star}$ and $E(B-V)_{\rm gas}$ on regional properties (panels from top to bottom): $\log_{10}t_L$, $\log_{10}\Sigma_{\rm H\alpha}$, and $\log_{10}$([N II]/[S II]). Panels in the leftmost column show the diagram of $E(B-V)_{\rm star}$ vs. $E(B-V)_{\rm gas}$ for all the ionized gas regions in our sample, with contours showing the distribution of the corresponding property. Panels from the second to the last column show the correlation of $E(B-V)_{\rm star}$, $E(B-V)_{\rm gas}$, $E(B-V)_{\rm gas}-E(B-V)_{\rm star}$ and $E(B-V)_{\rm star}/E(B-V)_{\rm gas}$ as functions of the property. The distributions of all the ionized gas regions are plotted as the gray-scale background in each panel, and the median relation and the 1σ scatter are plotted as the cyan lines. The median relation and the 1σ scatter of the subset of H II regions selected by $\log_{10}\Sigma_{\rm H\alpha}>39$ are additionally plotted as the dashed blue lines. The Spearman rank correlation coefficients (ρ) for both the full sample (black) and the H II regions (blue) are indicated.

Unlike $E(B-V)_{\rm star}$, the attenuation in gas, $E(B-V)_{\rm gas}$, shows strong correlations with multiple properties, including [N II]/[S II] ($\rho=0.58$) and $\Sigma_{\rm H\alpha}$ ($\rho=0.482$), as shown in Figure 3, and Σ_* ($\rho=0.432$), as shown in Appendix A. From the second row of Figure 3, we can see that both $E(B-V)_{\rm star}$ and $E(B-V)_{\rm gas}$ are correlated with $\Sigma_{\rm H\alpha}$, but in different ways at both the high and low end of $\Sigma_{\rm H\alpha}$. For regions with $\log_{10}\Sigma_{\rm H\alpha}\gtrsim 39$, which are dominated by H II regions, the two attenuation parameters behave quite similarly, showing positive correlations with $\Sigma_{\rm H\alpha}$. As a result, both their difference and ratio show a weak correlation with $\Sigma_{\rm H\alpha}$. The $E(B-V)_{\rm gas}-E(B-V)_{\rm star}$ increases slightly from $\sim$0.1 mag at $\log_{10}\Sigma_{\rm H\alpha}=39$ up to $\sim$0.25 mag at the highest $\Sigma_{\rm H\alpha}$. The $E(B-V)_{\rm star}/E(B-V)_{\rm gas}$ is almost constant at the value of 0.44 (Calzetti et al. 2000), ranging from $\sim$0.4 at $\log_{10}\Sigma_{\rm H\alpha}=39$ to $\sim$0.5 at $\log_{10}\Sigma_{\rm H\alpha}=41$, with small scatter. At $\log_{10}\Sigma_{\rm H\alpha}\lesssim 39$ where the regions are dominated by DIG, $E(B-V)_{\rm star}$ shows no obvious correlation with $\Sigma_{\rm H\alpha}$, with an average of $\sim$0.1 mag and large scatter, while $E(B-V)_{\rm gas}$ rapidly increases with increasing $\Sigma_{\rm H\alpha}$. Consequently, the $E(B-V)_{\rm gas}-E(B-V)_{\rm star}$ increases and the $E(B-V)_{\rm star}/E(B-V)_{\rm gas}$ decreases as the $\Sigma_{\rm H\alpha}$ increases. At the lowest density, $\log_{10}\Sigma_{\rm H\alpha}\lesssim 38.5$, the stellar attenuation is stronger than the gas attenuation, mainly because of the small amount of dust in the gas, as seen from the rapid decrease of $E(B-V)_{\rm gas}$ in the low-density end. The negative correlation of $E(B-V)_{\rm star}/E(B-V)_{\rm gas}$ with $\Sigma_{\rm H\alpha}$ has recently been discussed in depth in Lin & Kong (2020), based on an earlier sample of MaNGA. Our results show in addition that the correlation is essentially a result of the dichotomy of the intrinsic properties of the ionized gas regions, H II regions, and DIG regions, divided at $\Sigma_{\rm H\alpha}\sim 10^{39}$ erg s^{-1} kpc^{-2}, as suggested by Zhang et al. (2017). It is clear that H II regions and DIG regions are distinct in terms of the dust attenuation, in the sense that H II regions with higher $\Sigma_{\rm H\alpha}$ tend to be more dusty and have a tighter correlation between the stellar and gas attenuation. It is thus necessary to consider the two types of regions separately when their dust properties are studied.

The bottom row of Figure 3 shows the relation between [N II]/[S II] and the four dust attenuation parameters. Both a strong correlation with the gas attenuation and the absence of correlation with the stellar attenuation can be clearly seen. For the gas attenuation, the strong correlation is seen only when [N II]/[S II] exceeds $\sim$−0.2. In addition, noticeable correlations between gas attenuation and the gas-phase metallicity or related parameters are also found: $\rho=0.445$ for $12+\log_{10}$(O/H) and $\rho=-0.461$ for [O III]/[O II] (see Appendix A), which may share the same origin with the correlation with Σ_* given the well-known mass–metallicity relation (Tremonti et al. 2004). Similar to [N II]/[S II], the [O III]/[O II] also shows no correlation with the stellar attenuation, but a strong correlation with the gas attenuation (see Appendix A). Both [N II]/[S II] and [O III]/[O II] have been used as indicators of the ionization level of gas (Dopita et al. 2013; Lin & Kong 2020). In the ionization model of spherical H II regions from Dopita et al. (2013), the line ratio of [O III]/[O II] increases as the ionization parameter (q) increases when the gas-phase metallicity diagnostics (e.g., [N II]/[O II]) are fixed. Based on the same models and the MaNGA data, Lin & Kong (2020) found the line ratio [N II]/[S II] to be sensitive to both the gas-phase metallicity and the ionization parameter, with lower values of [N II]/[S II] in metal-poorer regions at fixed q. Note that $E(B-V)_{\rm gas}$ is also moderately correlated with D_n4000 ($\rho=0.386$) and $\log_{10}M_*$ ($\rho=0.459$). The former may be related to its correlation with stellar age as mentioned above, while the latter may be a result of its correlation with Σ_*.

In conclusion, we find that the stellar attenuation is mostly driven by stellar age, while the gas attenuation is most strongly related to $\Sigma_{\rm H\alpha}$, [N II]/[S II] and [O III]/[O II]. In the latter case, $\Sigma_{\rm H\alpha}$ divides ionized gas regions into two distinct types, DIG regions and H II regions, and [N II]/[S II] and [O III]/[O II] are indicators of the gas-phase metallicity and ionization level. For

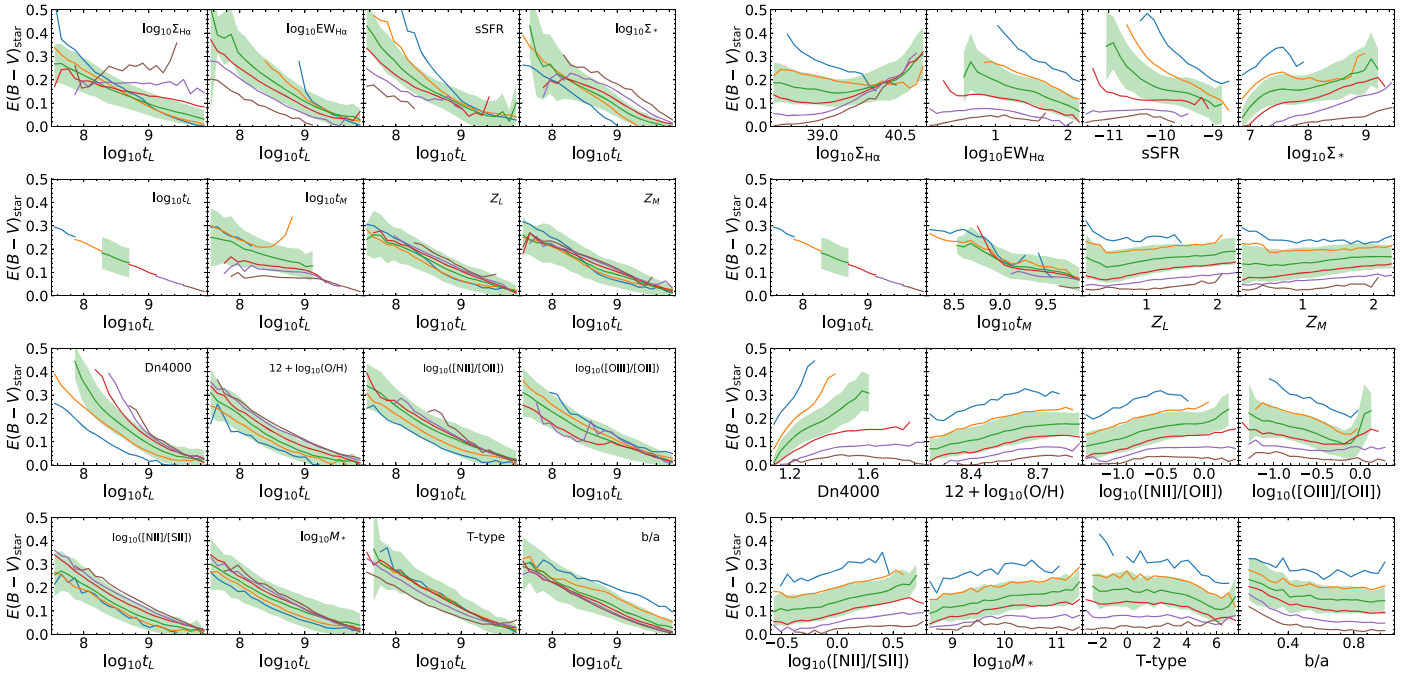

(a) $E(B-V)_{\rm star}$ versus $\log_{10}t_L$ (b) $E(B-V)_{\rm star}$ versus regional/global properties

Figure 4. Panels (a): $E(B-V)_{\rm star}$ as a function of $\log_{10}t_L$. In each panel the different colors show subsets of ionized gas regions selected by one of the 16 regional/global properties as indicated. Cyan, orange, green, red, purple, and brown correspond to subsets with increasing property values. For clarity, we only show the scatter of the green line as the scatters of other lines are comparable to that of the green line. Panels (b): $E(B-V)_{\rm star}$ as a function of regional and global properties. In each panel the different colors show ionized gas regions in different intervals of $\log_{10}t_L$. The stellar age binning can be seen from the leftmost panel in the second row.

the stellar-to-gas attenuation ratio (or difference), both stellar age and $\Sigma_{\rm H\alpha}$ play important roles. In the following subsections, we discuss these findings further. We focus on the stellar age versus stellar attenuation relation in Section 3.2, the role of $\Sigma_{\rm H\alpha}$, [N II]/[S II] and [O III]/[O II] for the gas attenuation in Section 3.3, and the joint role of $\log_{10}t_L$ and $\Sigma_{\rm H\alpha}$ for the stellar-to-gas attenuation ratio in Section 3.4.

3.2. The Role of Stellar Age in Driving Stellar Attenuation

In this subsection we concentrate on t_L, which has the strongest correlation with $E(B-V)_{\rm star}$ when compared to any other regional/global properties. This implies the potentially dominant role of the stellar age in driving the dust attenuation parameters. In order to test this hypothesis, we divide the ionized gas regions into different intervals of $\log_{10}t_L$ and examine the correlations of $E(B-V)_{\rm star}$ with other regional/global properties. Similarly, for a given regional/global property, we divide the ionized regions into intervals of the property and examine the correlations of the dust attenuation parameters with $\log_{10}t_L$. The results are shown in Figure 4.

Panels (a) of Figure 4 show the correlation of $E(B-V)_{\rm star}$ with $\log_{10}t_L$, but for the subsets of ionized gas regions selected by each of the regional/global properties. Panels (b) show the correlation of $E(B-V)_{\rm star}$ with different regional/global properties, but for the subsets of ionized gas regions selected by $\log_{10}t_L$. In most cases, $E(B-V)_{\rm star}$ shows tight correlations with $\log_{10}t_L$ even when the sample is limited to a narrow range of a specific property, as can be seen from panels (a), while $E(B-V)_{\rm star}$ shows no or a rather weak dependence on all other properties once the stellar age is limited to a narrow range, as shown in panels (b). This result reinforces the conclusion from the previous subsection that the stellar attenuation is predominantly driven by the stellar age.

One can identify two subsets of the ionized gas regions in which residual correlations are clearly seen. The subset, which consists of the regions with both high Hα surface brightness ($\Sigma_{\rm H\alpha}\gtrsim 10^{39}\,{\rm erg\,s^{-1}\,kpc^{-2}}$) and old stellar ages ($t_L\gtrsim$1Gyr), shows that the $E(B-V)_{\rm star}$ is more strongly correlated with $\Sigma_{\rm H\alpha}$ than with $\log_{10}t_L$. This can be seen from the top left panel in both panels (a) and (b) of the figure. The second subset, consisting of regions with very young ages (with t_L lower than a few $\times 10^8$ yr), shows residual correlations with D_n4000 (as well as with $\rm EW_{H\alpha}$ and sSFR) at fixed $\log_{10}t_L$.

We repeated the same analysis for $E(B-V)_{\rm gas}-E(B-V)_{\rm star}$ and $E(B-V)_{\rm star}/E(B-V)_{\rm gas}$, and the results are presented in Appendix B. We see that the stellar age is correlated with both $E(B-V)_{\rm gas}-E(B-V)_{\rm star}$ and $E(B-V)_{\rm star}/E(B-V)_{\rm gas}$ in most cases when other properties are fixed, while at fixed $\log_{10}t_L$, no strong correlation is seen between either of the attenuation parameters and other properties. These behaviors can be attributed largely to the correlation between $E(B-V)_{\rm star}$ and $\log_{10}t_L$, as shown in Figure 4.

3.3. The Role of $\Sigma_{\rm H\alpha}$, [N II]/[S II] and [O III]/[O II] in Driving Gas Attenuation

Similarly, we have compared the dependence of $E(B-V)_{\rm gas}$ on $\Sigma_{\rm H\alpha}$, [N II]/[S II] and [O III]/[O II] with that on other regional/global properties. We find that of the three properties, [N II]/[S II] shows stronger correlations with $E(B-V)_{\rm gas}$ than either $\Sigma_{\rm H\alpha}$ and [O III]/[O II] when other properties are limited to a narrow range. This is consistent with the fact that the highest correlation efficient is between $E(B-V)_{\rm gas}$ and [N II]/[S II]

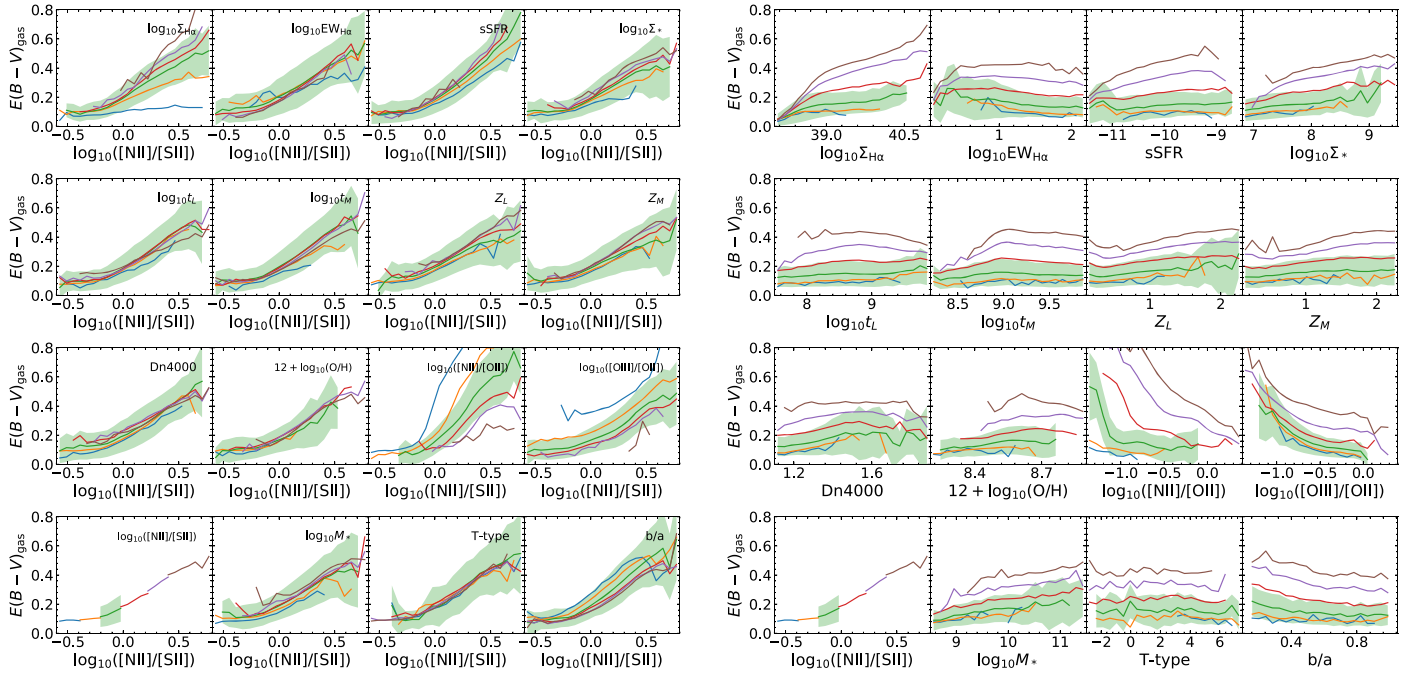

(a) $E(B-V)_{\rm gas}$ versus $\log_{10}([\rm N\,II]/[\rm S\,II])$ (b) $E(B-V)_{\rm gas}$ versus regional/global properties

Figure 5. $E(B-V)_{\rm gas}$ as function of $\log_{10}([\rm N\,II]/[\rm S\,II])$ for subsets of ionized gas regions selected by each of the 16 regional/global properties as indicated (panels (a)), and as functions of regional/global properties for subsets of ionized gas regions selected by $\log_{10}([\rm N\,II]/[\rm S\,II])$ (panels (b)). Symbols and lines are the same as in Figure 4.

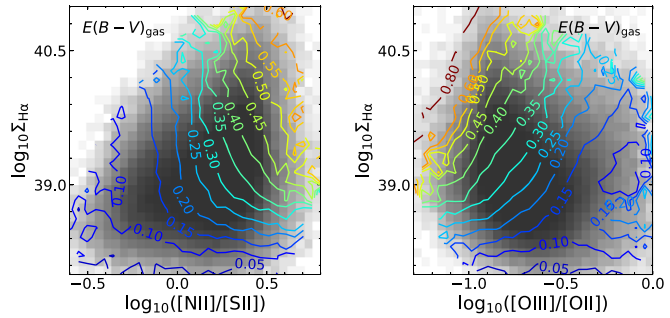

Figure 6. Distributions of all the ionized gas regions in the plane of $\log_{10}\Sigma_{\rm H\alpha}$ vs. $\log_{10}([\rm N\,II]/[\rm S\,II])$ (left panel) and the plane of $\log_{10}\Sigma_{\rm H\alpha}$ vs. $\log_{10}([\rm O\,III]/[\rm O\,II])$ (right panel) are plotted as the gray-scale background, while contours of $E(B-V)_{\rm gas}$ are plotted as colored lines, and the contour levels are indicated.

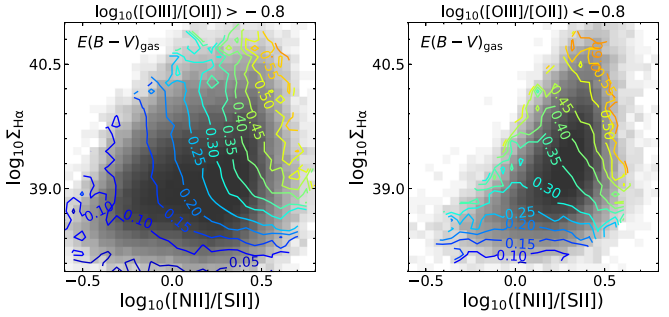

Figure 7. Distribution on the plane of $\log_{10}\Sigma_{\rm H\alpha}$ vs. $\log_{10}([\rm N\,II]/[\rm S\,II])$ for ionized gas regions with $\log_{10}([\rm O\,III]/[\rm O\,II]) > -0.8$ (left panel) and those with $\log_{10}([\rm O\,III]/[\rm O\,II]) < -0.8$ (right panel). Symbols and lines are the same as in Figure 6.

(see Section 3.1). We therefore only show the results for [N II]/[S II] in Figure 5 and present the results for $\Sigma_{\rm H\alpha}$ and [O III]/[O II] in Appendix B.

As can be seen from Figure 5, the gas attenuation is positively correlated with [N II]/[S II] when other properties are fixed, but this is true only for H II regions with $\Sigma_{\rm H\alpha} \gtrsim 10^{39}\,{\rm erg\,s^{-1}\,kpc^{-2}}$. This result echoes the $\Sigma_{\rm H\alpha}$ dichotomy, as discussed above. For DIG regions with lower $\Sigma_{\rm H\alpha}$, the gas attenuation shows a weak dependence on [N II]/[S II] (see the top left panel of panels (a)), and strong dependence on $\Sigma_{\rm H\alpha}$ when [N II]/[S II] is fixed (see the top left panel of panels (b)). Apparently, [N II]/[S II] plays a dominant role for H II regions, showing strong correlations with $E(B-V)_{\rm gas}$ in almost all cases when the regional/global properties, including $\Sigma_{\rm H\alpha}$ are fixed (panels (a)). No residual correlation of $E(B-V)_{\rm gas}$ is seen for most of the regional/global properties if $\log_{10}([\rm N\,II]/[\rm S\,II])$ is fixed (panels (b)). Two properties, [N II]/[O II] and [O III]/[O II], show residual correlations with $E(B-V)_{\rm gas}$ at fixed $\log_{10}([\rm N\,II]/[\rm S\,II])$. This is probably not surprising. As found in Lin & Kong (2020), [N II]/[S II] is sensitive to both gas-phase metallicity and the ionized level of the gas, and thus it is expected to correlate with both [N II]/[O II], which is a metallicity indicator, and [O III]/[O II], which is an indicator of the ionized level.

Figure 5 suggests that the $E(B-V)_{\rm gas}$ is determined mainly by two parameters: $\Sigma_{\rm H\alpha}$ for DIG regions with low $\Sigma_{\rm H\alpha}$, and [N II]/[S II] for H II regions with high $\Sigma_{\rm H\alpha}$. This finding is more clearly seen in Figure 6 (left panel), where we show the contours of $E(B-V)_{\rm gas}$ in the diagram of $\log_{10}\Sigma_{\rm H\alpha}$ versus $\log_{10}([\rm N\,II]/[\rm S\,II])$. Below $\log_{10}\Sigma_{\rm H\alpha} \sim 39$, the contours are almost horizontal, and so the change of $E(B-V)_{\rm gas}$ is mainly driven by $\Sigma_{\rm H\alpha}$. Above $\log_{10}\Sigma_{\rm H\alpha} \sim 39$, in contrast, the contours are largely vertical, indicating that $E(B-V)_{\rm gas}$ is driven mainly by $\log_{10}([\rm N\,II]/[\rm S\,II])$. In the right panel of the same figure, we show the contours of $E(B-V)_{\rm gas}$ in the $\log_{10}\Sigma_{\rm H\alpha}$ versus $\log_{10}([\rm O\,III]/[\rm O\,II])$ plane. Below $\log_{10}\Sigma_{\rm H\alpha} \sim 39$, again,

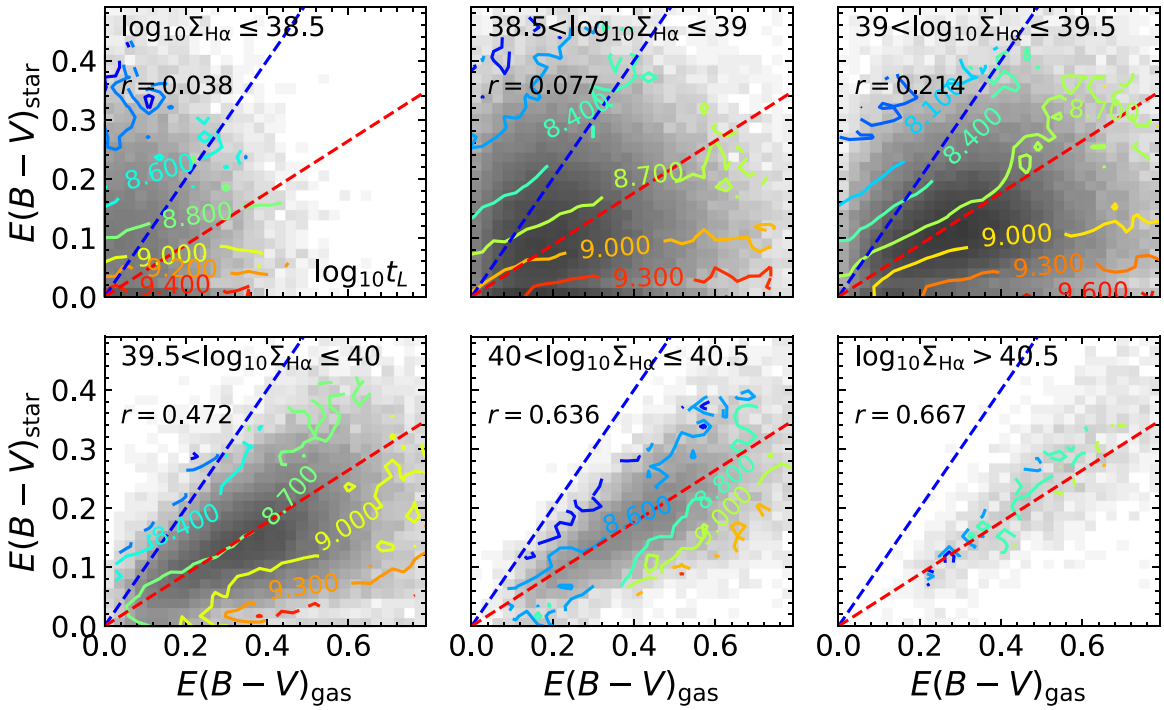

Figure 8. $E(B-V)_{\rm star}$ vs. $E(B-V)_{\rm gas}$ in different intervals of $\Sigma_{\rm H\alpha}$. The colored lines are the contours of $\log_{10}t_L$ as indicated, and the gray-scale background shows the number density distribution of the ionized gas regions in each $\Sigma_{\rm H\alpha}$ bin. The dashed blue line is the 1:1 relation, and the dashed red line represents the relation of $E(B-V)_{\rm star}=0.44\,E(B-V)_{\rm gas}$. The Pearson linear correlation coefficient (r) between the two attenuations is indicated in each panel.

the $E(B-V)_{\rm gas}$ is mainly driven by $\Sigma_{\rm H\alpha}$ with no correlation with [O III]/[O II]. At higher $\Sigma_{\rm H\alpha}$, the contours are inclined, indicating that neither $\Sigma_{\rm H\alpha}$ nor [O III]/[O II] alone can dominate in the $E(B-V)_{\rm gas}$. At fixed $\Sigma_{\rm H\alpha}$, the correlation of $E(B-V)_{\rm gas}$ with [O III]/[O II] appears to be weaker in regions with $\log_{10}$([O III]/[O II]) $\gtrsim -0.8$ than in lower ionization regions.

Figure 7 displays the $\Sigma_{\rm H\alpha}$–[N II]/[S II] relation again, but separately for high- and low-ionization regions divided at $\log_{10}$([O III]/[O II]) $=-0.8$. The high-ionization regions (left panel) cover almost the full range in the diagram, and the contours in H II regions (high $\Sigma_{\rm H\alpha}$) and with high [N II]/[S II] (high metallicity) become more vertical when compared to those for the full sample, suggesting that the diagnostic of [O III]/[O II] in these regions may be negligible. This is consistent with the weak correlation of $E(B-V)_{\rm gas}$ with [O III]/[O II] at $\log_{10}$([O III]/[O II]) $\gtrsim -0.8$ seen in the right panel of Figure 6. Low-ionization regions (right panel) are distributed differently: they are either DIG regions spanning all the range of [N II]/[S II], or they are limited to H II regions of high [N II]/[S II]. In the latter case, the $E(B-V)_{\rm gas}$ depends jointly on $\Sigma_{\rm H\alpha}$ and [N II]/[S II], as indicated by the inclined contours. Apparently, the diagnostic of [O III]/[O II] cannot be neglected for low-ionization H II regions.

3.4. Dependence of $\rm E(B-V)_{star}/E(B-V)_{gas}$ on both $\Sigma_{H\alpha}$ and $\rm t_L$

In this subsection we focus on the stellar-to-gas attenuation ratio, $E(B-V)_{\rm star}/E(B-V)_{\rm gas}$. The analysis so far has revealed that the stellar age is the property that is most strongly correlated with $E(B-V)_{\rm star}/E(B-V)_{\rm gas}$ (see Figure 3), and that the $\Sigma_{\rm H\alpha}$ plays an important role as well. The residual dependence on $\Sigma_{\rm H\alpha}$ at fixed $\log_{10}t_L$ can largely be attributed to the dichotomy of the ionized gas regions. Thus, all the regions can be well divided into H II regions with high $\Sigma_{\rm H\alpha}$ and DIG regions with low $\Sigma_{\rm H\alpha}$. In this subsection we study the dependence of $E(B-V)_{\rm star}/E(B-V)_{\rm gas}$ on $\Sigma_{\rm H\alpha}$ and t_L jointly.

Figure 8 shows the distribution of the ionized regions in the $E(B-V)_{\rm star}$ versus $E(B-V)_{\rm gas}$ plane, but for six successive, nonoverlapping intervals of $\log_{10}\Sigma_{\rm H\alpha}$. In each $\log_{10}\Sigma_{\rm H\alpha}$ interval, the distribution of the ionized gas regions is plotted in gray scales, overlaid with colored contours of $\log_{10}t_L$. The Pearson linear correlation coefficient is also indicated in each panel. For DIG regions with $\log_{10}\Sigma_{\rm H\alpha}\lesssim 39$, the correlation coefficient is close to zero, indicative of no correlation. At fixed $E(B-V)_{\rm gas}$, $E(B-V)_{\rm star}$ spans the full range from zero up to $\sim$0.5 mag, while $E(B-V)_{\rm gas}$ is limited to relatively low values with the upper limit increasing from $\sim$0.2 mag at $\log_{10}\Sigma_{\rm H\alpha}\leqslant 38.5$ to $\sim$0.6 mag at $38.5<\log_{10}\Sigma_{\rm H\alpha}\leqslant 39$. For H II regions, as $\Sigma_{\rm H\alpha}$ increases, the correlation between the two $E(B-V)$ measurements becomes increasingly evident, and the scatter decreases steadily. The average relation of the H II regions follows the relation $E(B-V)_{\rm star}=0.44\,E(B-V)_{\rm gas}$, which is indicated by the dashed red line in each panel. When $\log_{10}\Sigma_{\rm H\alpha}$ exceeds $\sim$39.5, almost all the regions fall below the 1:1 relation.

When $\log_{10}t_L$ is fixed, $E(B-V)_{\rm star}$ is linearly correlated with $E(B-V)_{\rm gas}$, and this is true in all the different $\log_{10}\Sigma_{\rm H\alpha}$ intervals, although the slope and intercept of the linear relation vary with both $\log_{10}t_L$ and $\log_{10}\Sigma_{\rm H\alpha}$. To quantify the joint dependence on $\log_{10}\Sigma_{\rm H\alpha}$ and $\log_{10}t_L$, we perform a linear fitting to the relation between $E(B-V)_{\rm star}$ and $E(B-V)_{\rm gas}$ for given $\log_{10}t_L$ and $\log_{10}\Sigma_{\rm H\alpha}$. For each $\log_{10}\Sigma_{\rm H\alpha}$ bin, the ionized gas regions are sorted by increasing $\log_{10}t_L$ and are divided into a number of $\log_{10}t_L$ bins by requiring each bin to contain 200 ionized gas regions. A linear relation is obtained by fitting the

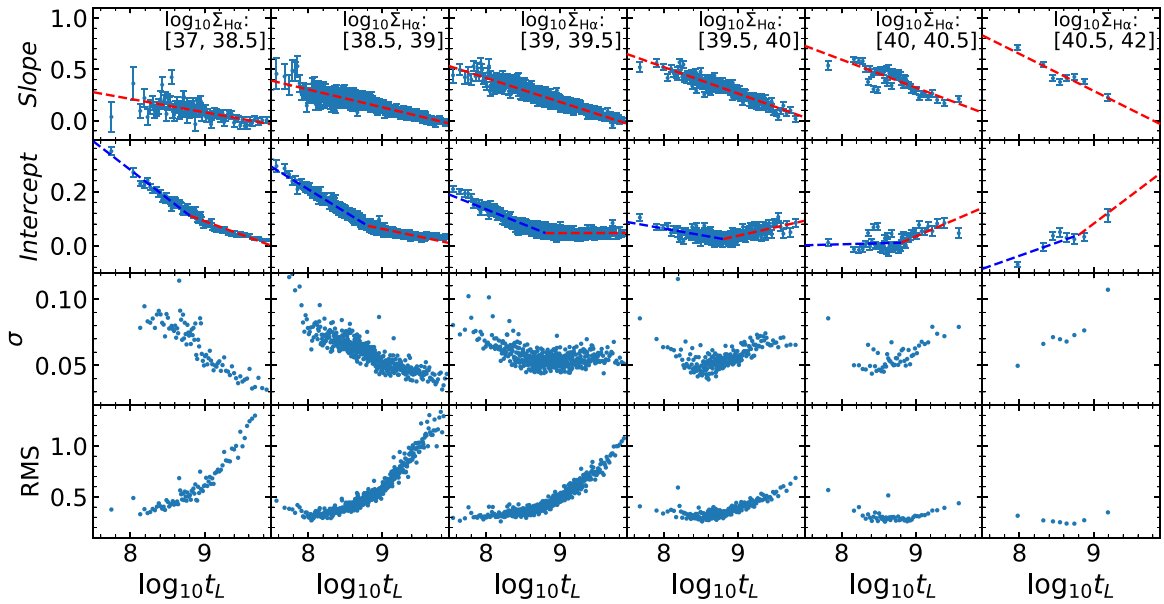

Figure 9. The upper two rows show the slope and intercept of the relation in Equation (3) as a function of $\log_{10}t_L$ for different intervals of $\log_{10}\Sigma_{\rm H\alpha}$. In each panel, the dashed red and blue lines are the best-fit model. The third row shows the standard deviation of ionized gas regions around the best-fit relation (σ), while the bottom row shows the rms of the relative difference of the ionized gas regions from the best-fit relation (σ/best-fit). See text for details.

Table 1
Best-fit Coefficients in Equations (4) and (5) that Describe the Slope and Intercept of the Stellar-to-gas Attenuation Linear Relation as a Function of Luminosity-weighted Stellar Age

$\log_{10}\Sigma_{\rm H\alpha}$	a_0	b_0	a_1	b_1	a_2	b_2
(38.5]	−0.130	1.253	−0.211	1.968	−0.101	0.996
(38.5, 39.0]	−0.174	1.692	−0.168	1.553	−0.058	0.582
(39.0, 39.5]	−0.234	2.286	−0.110	1.012	0.0006	0.041
(39.5, 40.0]	−0.257	2.576	−0.049	0.452	0.062	−0.520
(40.0, 40.5]	−0.271	2.766	0.007	−0.052	0.118	−1.024
(40.5,]	−0.360	3.527	0.097	−0.812	0.207	−1.783

following equation to the data in each bin,

$$E(B-V)_{\rm star} = {\rm Slope} \times E(B-V)_{\rm gas} + {\rm Intercept}. \quad (3)$$

The upper two panels in Figure 9 show the best-fit slope and intercept as functions of $\log_{10}t_L$, for different $\log_{10}\Sigma_{\rm H\alpha}$ bins. Overall, the relations are quite flat at the lowest $\Sigma_{\rm H\alpha}$ and the highest t_L, with a slope close to zero for regions with $\log_{10}\Sigma_{\rm H\alpha} < 38.5$ and t_L older than a few billion years. The slope increases with $\Sigma_{\rm H\alpha}$ at fixed t_L and decreases with t_L at fixed $\Sigma_{\rm H\alpha}$. The intercept behaves differently for young regions with $t_L \lesssim 1$ Gyr and old regions with higher t_L. For the young regions, the intercept decreases with both t_L and $\Sigma_{\rm H\alpha}$, while for the old regions, the intercept decreases with t_L in DIG regions and increases with t_L in H II regions. For DIG regions, the small slope suggests a poor correlation between $E(B-V)_{\rm star}$ and $E(B-V)_{\rm gas}$. In H II regions, the intercept is relatively small, close to zero in H II regions with $\log_{10}\Sigma_{\rm H\alpha} > 39.5$. The slope is thus approximately equal to $E(B-V)_{\rm star}/E(B-V)_{\rm gas}$ for these H II regions, with a value comparable to the average of $E(B-V)_{\rm star}/E(B-V)_{\rm gas} \approx 0.44$, but varying with both t_L and $\Sigma_{\rm H\alpha}$.

The lower two panels of Figure 9 show the standard deviation of the ionized gas regions around the best-fit relation and the rms of their relative difference from the best-fit relation. The scatter of the ionized regions around the $E(B-V)_{\rm star}$ versus $E(B-V)_{\rm gas}$ relations depends on $\Sigma_{\rm H\alpha}$ and t_L in a way similar to the dependence of the intercept on these two parameters. Overall, the scatter is smaller than 0.1 mag in all cases, and it is relatively large for DIG regions of young ages ($\Sigma_{\rm H\alpha} \lesssim 10^{39}$ erg s^{-1} kpc^{-2} and $t_L \lesssim 1$ Gyr) and for high-$\Sigma_{\rm H\alpha}$ H II regions of old ages ($\Sigma_{\rm H\alpha} \gtrsim 10^{40}$ erg s^{-1} kpc^{-2} and $t_L \gtrsim 1$ Gyr), ranging from 0.05 mag to 0.1 mag. The rms of the relative difference from the best-fit relations decreases with increasing $\Sigma_{\rm H\alpha}$, and it is smaller than 50% at ages younger than ~1 Gyr with a weak dependence on t_L. At older ages, the rms is only 20%–30% at the highest $\Sigma_{\rm H\alpha}$ (>10^{40} erg s^{-1} kpc^{-2}), but increases rapidly toward lower $\Sigma_{\rm H\alpha}$. The large rms at the low $\Sigma_{\rm H\alpha}$ again reflects the poor correlations between the stellar and gas attenuation in the DIG regions.

As can be seen from Figure 9, both slope and intercept depend on $\log_{10}t_L$ in a rather simple way. For a given $\Sigma_{\rm H\alpha}$ range, we model slope and intercept as function of $\log_{10}t_L$ using

$$\text{Slope} = a_0 \times \log_{10}t_L + b_0, \quad (4)$$

and

$$\text{Intercept} = \begin{cases} a_1 \times \log_{10}t_L + b_1, \text{ if } \log_{10}t_L \leqslant 8.8 \\ a_2 \times \log_{10}t_L + b_2, \text{ if } \log_{10}t_L > 8.8. \end{cases} \quad (5)$$

The best-fit relations are plotted in Figure 9 as the dashed lines, and the best-fit values of a_0, b_0, a_1, b_1, a_2, and b_2 are listed in Table 1 for the different intervals of $\Sigma_{\rm H\alpha}$.

4. Discussion

4.1. Comparison with Previous MaNGA-based Studies

Recently, Lin & Kong (2020) and Greener et al. (2020) have used the MaNGA data to study the dust attenuation in nearby galaxies. In this subsection we compare our work with the two studies. We note that in a recent study based on MaNGA, Riffel et al. (2021) also examined the correlation between $E(B-V)_{\rm star}$ and $E(B-V)_{\rm gas}$, but focusing on AGN host galaxies and a control sample of star-forming galaxies. Here we do not make comparisons with this study because the sample selection is different.

4.1.1. Comparison with Lin & Kong (2020)

Lin & Kong (2020) used the dust attenuation parameters and spectroscopic properties from the MaNGA value-added catalog produced by applying the Pipe3D pipeline (Sánchez et al. 2018) to the SDSS DR15, which contains ∼4800 data cubes from MaNGA. Pipe3D performed spatial binning for each data cube and fit the binned spectra with a set of simple stellar population models (González Delgado et al. 2005; Vazdekis et al. 2010; Cid Fernandes et al. 2013). The dust attenuation curve of Cardelli et al. (1989) and a selective extinction of $R_V = 3.1$ were assumed, and a stellar attenuation was determined as one of the free parameters in the spectral fitting.

The authors examined the correlation between $E(B-V)_{\rm star}$ and $E(B-V)_{\rm gas}$, and the dependence on a variety of galaxy properties, both regional and global. In particular, they found that both the Pearson and Spearman rank correlation coefficients increase rapidly with $\log_{10}\Sigma_{\rm H\alpha}$, from <0.1 at $\log_{10}\Sigma_{\rm H\alpha} < 39$ up to ∼0.8 at $\log_{10}\Sigma_{\rm H\alpha} > 40.5$ (see their Figure 2). This dependence is also seen in our results, e.g., in Figure 8. We further find that the scatter in the relation between $E(B-V)_{\rm star}$ and $E(B-V)_{\rm gas}$ at fixed $\Sigma_{\rm H\alpha}$ can be well explained by the stellar age, which can also be seen from Figure 8. When they are limited to a narrow range of $\log_{10}t_L$, the two attenuation parameters are linearly correlated, although the slope, intercept and scatter of the relation vary with $\Sigma_{\rm H\alpha}$ and t_L. We show that the variations can be described quantitatively by simple functions (see Figure 9 and Table 1).

Lin & Kong (2020) payed particular attention to $E(B-V)_{\rm star}/E(B-V)_{\rm gas}$, finding it to be larger in DIG regions than in H II regions, which is also found from our data (see Figure 3). According to the Spearman rank correlation analysis, they found that $E(B-V)_{\rm star}/E(B-V)_{\rm gas}$ is the most strongly correlated with $\log_{10}$([N II]/[S II]), with a correlation coefficient close to $\rho = -0.5$, and it is the least strongly correlated with D_n4000, with $\rho \sim -0.1$ (see their Figure 3). In contrast, we find that among other properties, the luminosity-weighted stellar age t_L is the property that shows the strongest correlation with $E(B-V)_{\rm star}/E(B-V)_{\rm gas}$, with $\rho = -0.63$ (see Figure 3). The Spearman correlation coefficient is $\rho = -0.38$ between $E(B-V)_{\rm star}/E(B-V)_{\rm gas}$ and D_n4000, not as weak as found in Lin & Kong (2020). The different correlation coefficient for D_n4000 may be attributed to the different data products used in the two studies. In fact, we have repeated the analysis of the correlation between $E(B-V)_{\rm star}/E(B-V)_{\rm gas}$ and D_n4000 using measurements from the Pipe3D VAC, and found a similarly weak correlation.

In Section 3.1 we have discussed the dominant role of the stellar age in driving $E(B-V)_{\rm star}$, as well as its difference and ratio relative to $E(B-V)_{\rm gas}$. This analysis was missing in Lin & Kong (2020) for two reasons. First, the authors did not consider the stellar age directly, but adopted D_n4000 as an indicator of it. The D_n4000 is indeed a good indicator of stellar age, but sensitive only to populations younger than 1–2 Gyr (Bruzual & Charlot 2003; Kauffmann et al. 2003b). Second, our measurements of $E(B-V)_{\rm star}$ are more reliable and accurate than in previous studies because we use the new technique of measuring stellar attenuation developed in Paper I. As shown in Appendix B of Paper I, our method can obtain $E(B-V)_{\rm star}$ before the stellar population is modeled, thus significantly alleviating the degeneracy between dust attenuation and stellar population properties, such as stellar age and metallicity. We have used data from the Pipe3D VAC and found the Spearman rank correlation coefficient to be $\rho = -0.3$ between $E(B-V)_{\rm star}/E(B-V)_{\rm gas}$ and $\log_{10}t_L$. Thus, the dominant role of the stellar age would be missed in our analysis if the stellar attenuation and age measurements were not improved substantially.

We find that the Spearman correlation coefficient between $E(B-V)_{\rm star}/E(B-V)_{\rm gas}$ and [N II]/[S II] is $\rho = -0.36$ (see Figure 3), weaker than the coefficient of $\rho \sim -0.5$ found in Lin & Kong (2020). Again, using the Pipe3D data, we obtain $\rho = -0.49$, in good agreement with their result. Assuming the relevant emission lines are measured reasonably well in the two studies, we conclude that the different correlation coefficients for the relation of $E(B-V)_{\rm star}/E(B-V)_{\rm gas}$ with [N II]/[S II] are caused mainly by the different measurements of $E(B-V)_{\rm star}$. Our $E(B-V)_{\rm star}$ measurements are expected to be more reliable for the reasons mentioned above. On the other hand, we find that [N II]/[S II] is indeed one of the dominant parameters for $E(B-V)_{\rm gas}$, as discussed in Section 3.1, and it drives the gas attenuation in H II regions. Furthermore, we confirm the finding of Lin & Kong (2020) that the ionization level of the gas as indicated by [O III]/[O II] cannot be simply neglected, and we find that this parameter needs to be considered only in H II regions with low ionization, $\log_{10}$([O III]/[O II]) $\lesssim -0.8$.

To conclude, comparing with Lin & Kong (2020), we confirm the following results:

1. The relation between $E(B-V)_{\rm star}$ and $E(B-V)_{\rm gas}$ is stronger for more active H II regions;
2. Local physical properties such as metallicity and ionization level play important roles in determining the dust attenuation.

In addition, we obtain the following new results:

1. Stellar age is the driving factor for $E(B-V)_{\rm star}$ and consequently for $E(B-V)_{\rm gas} - E(B-V)_{\rm star}$ and $E(B-V)_{\rm star}/E(B-V)_{\rm gas}$.
2. At fixed $\Sigma_{\rm H\alpha}$, the stellar age is linearly correlated with $E(B-V)_{\rm star}/E(B-V)_{\rm gas}$ at all ages.
3. Gas-phase metallicity and ionization level are important, but only for the attenuation in $E(B-V)_{\rm gas}$.

4.1.2. Comparison with Greener et al. (2020)

Greener et al. (2020) have recently studied the spatially resolved dust attenuation in 232 spiral galaxies from the eighth MaNGA Product Launch (MPL-8) with morphological classifications from Galaxy Zoo:3D (Masters et al. 2021). The stellar dust attenuation was measured using the full-spectrum stellar population fitting code STARLIGHT (Cid Fernandes et al. 2005;

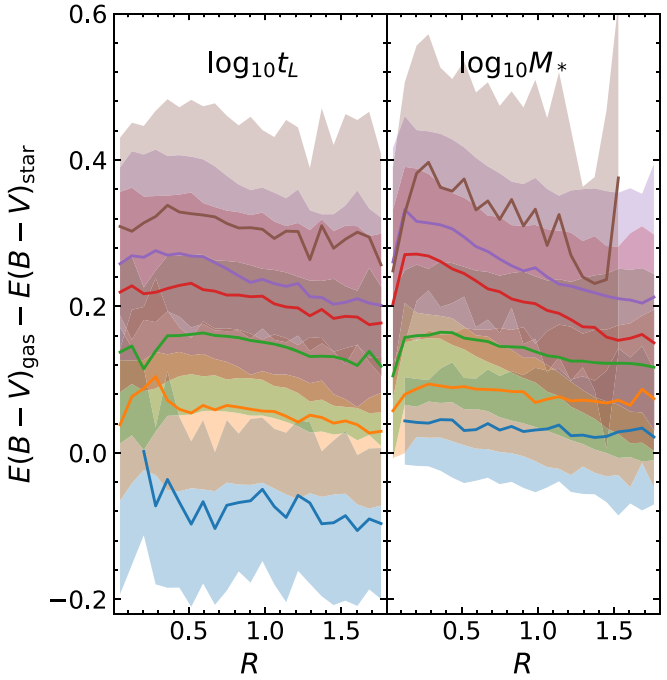

Figure 10. The median radial profiles of the gas-to-stellar attenuation difference for ionized gas regions with different $\log_{10}t_L$ (left panel) or $\log_{10}M_*$ (right panel). The shaded regions indicate the 1σ scatter of the regions around the median profile.

Cid Fernandes 2018), with SSPs from the E-MILES (Vazdekis et al. 2010, 2016) templates and a Calzetti et al. (2000) attenuation curve with $R_V = 4.05$, while the gas dust attenuation was measured from the Balmer decrement assuming $R_V = 3.1$.

The authors found that dust attenuation increases with $\Sigma_{\rm SFR}$ (SFR surface density), consistent with the positive correlations of both $E(B-V)_{\rm star}$ and $E(B-V)_{\rm gas}$ with $\Sigma_{\rm H\alpha}$ seen from Figure 3, and that the ratio $E(B-V)_{\rm star}/E(B-V)_{\rm gas}$ decreases with M_*, which is also seen from our data. They found that both $E(B-V)_{\rm star}$ and $E(B-V)_{\rm gas}$ decrease from the galactic center outward, which is also seen from our data. They also found that the ratio $E(B-V)_{\rm star}/E(B-V)_{\rm gas}$ has no correlation with the distance from galactic center (R), while our data show a weak correlation between $E(B-V)_{\rm star}/E(B-V)_{\rm gas}$ and R, with $\rho = 0.25$ for all the ionized gas regions and $\rho = 0.24$ for H II regions. In addition, Greener et al. (2020) found a high concentration of birth clouds near the galactic center, as indicated by a negative radial gradient in $E(B-V)_{\rm gas} - E(B-V)_{\rm star}$. As can be seen from Figure 10 (the right panel), our data also show these negative radial profiles at fixed stellar mass, and the gradient is stronger at higher mass. We find, however, that the gradient becomes rather weak when the ionized gas regions are limited to narrow ranges of $\log_{10}t_L$, as shown in the left panel of the same figure. Therefore the higher $E(B-V)_{\rm gas}-E(B-V)_{\rm star}$ at smaller R should be attributed to the positive correlation of $E(B-V)_{\rm gas}-E(B-V)_{\rm star}$ with stellar age (see Figure 3), given that the stellar populations in the inner regions of galaxies are typically older than those in the outer regions. We notice from Figure 10 a weak upturn within $\sim 0.5\,R_e$ in the $E(B-V)_{\rm gas} - E(B-V)_{\rm star}$ of the youngest regions. This may be explained if birth clouds are concentrated in the central regions of galaxies, as suggested by Greener et al. (2020), because very young stars are mostly embedded in birth clouds. However, this result should not be overemphasized, given that the upturn is weak and the noise level is high. We will revisit this in the future.

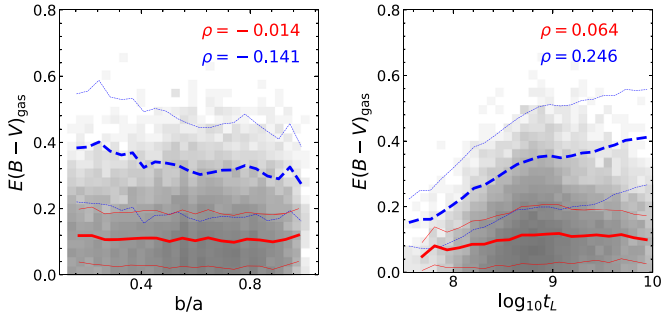

Figure 11. $E(B-V)_{\rm gas}$ as function of b/a (left) and $\log_{10}t_L$ (right) for DIG regions with $\Sigma_{\rm H\alpha} < 10^{38.5}$ erg s^{-1} kpc^{-2} (red lines) and H II regions with $\Sigma_{\rm H\alpha} < 10^{39}$ erg s^{-1} kpc^{-2} (blue lines). The number density distribution of the DIG regions is plotted as the gray-scale background. The solid lines are the median relations, and the dashed lines indicate the 1σ scatter of the DIG or H II regions around the median relation. The Spearman rank correlation coefficients are indicated for both types of regions, with red for DIG and blue for H II regions.

4.2. Implications of the Ionizing Source for DIG

We find that in DIG regions, $E(B-V)_{\rm star}$ is weakly correlated with $E(B-V)_{\rm gas}$ and in many cases $E(B-V)_{\rm star}$ is larger than $E(B-V)_{\rm gas}$. The behavior is very different from that for H II regions. H II regions are mostly located below the 1:1 relation in the $E(B-V)_{\rm star}$ versus $E(B-V)_{\rm gas}$ diagram and follow the $E(B-V)_{\rm star} = 0.44\,E(B-V)_{\rm gas}$ relation on average (Figure 8). For DIG regions, most of the scatter in the relation between $E(B-V)_{\rm star}$ and $E(B-V)_{\rm gas}$ can be explained by the variance in stellar age, as shown in Section 3.4 and Figure 9.

The different behaviors of the dust attenuation between DIG and H II regions imply that the emission in the two classes are produced by different mechanisms. The physical origin of the DIG is not clear. A variety of ionizing sources have been proposed for the DIG, including supernova shocks, cosmic rays, leaky radiation from H II regions, and hot evolved stars (e.g., Reynolds & Cox 1992; Haffner et al. 2009; Yan & Blanton 2012; Barnes et al. 2014, 2015; Zhang et al. 2017). Using MaNGA data, Zhang et al. (2017) examined the ionization and metallicity diagnostics of DIG-dominated regions, finding that DIG has a lower ionization level than H II regions, which can enhance [N II]/Hα, [S II]/Hα, [O II]/Hα, and [O II]/Hα, but reduce [O III]/Hβ. As the leaky H II region model cannot produce the LINER-like emission commonly seen in DIG regions, the authors suggested that hot evolved stars could be a major ionization source for DIG, at least in the following two cases: (1) low-surface brightness regions that are located far from H II regions, such as regions at large vertical height, and (2) post-starburst galaxies and quiescent galaxies.

Our data support the suggestion of Zhang et al. (2017). In Figure 11 we plot $E(B-V)_{\rm gas}$ as a function of both b/a and $\log_{10}t_L$ for DIG regions with $\Sigma_{\rm H\alpha} < 10^{38.5}$ erg s^{-1} kpc^{-2}. Here we use a $\Sigma_{\rm H\alpha}$ limit 0.5 dex smaller than the usually adopted value to reduce the contamination of the H II regions. For comparison, the results for the H II regions with $\Sigma_{\rm H\alpha} > 10^{39}$ erg s^{-1} kpc^{-2} are also plotted as solid and dashed blue lines. Overall, the DIG and H II regions behave quite differently in the sense that $E(B-V)_{\rm gas}$ depends on both b/a and $\log_{10}t_L$ in H II regions, but $E(B-V)_{\rm gas}$ shows no dependence on

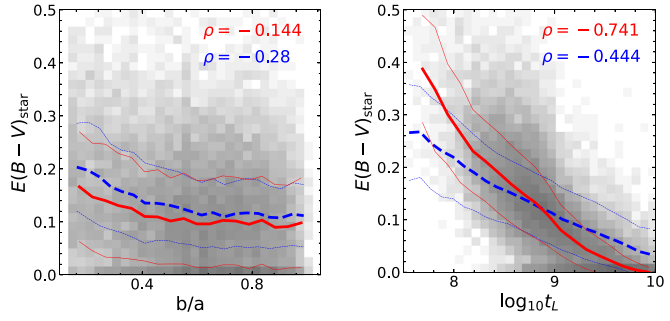

Figure 12. $E(B-V)_{\rm star}$ as a function of b/a (left) and $\log_{10}t_L$ (right) for DIG regions with $\Sigma_{\rm H\alpha} < 10^{38.5}$ erg s^{-1} kpc^{-2} (red lines) and H II regions with $\Sigma_{\rm H\alpha} > 10^{39}$ erg s^{-1} kpc^{-2} (blue lines). Symbols and lines are the same as in Figure 11.

either parameter in DIG regions. In addition, the median value of $E(B-V)_{\rm gas}$ in DIG regions is pretty low, constantly at $\sim$0.1 mag for all values of b/a and $\log_{10}t_L$. This weak gas attenuation in DIG regions and its independence of b/a strongly indicates that the ionizing source for DIG is distributed in the outskirts of galaxies, either at large vertical heights or at large radial distances, or both. Ionizing photons emerging from these locations can easily escape the galaxy without being attenuated much because of the short propagation path through the ISM, thus leading to $E(B-V)_{\rm gas}$ values that are low and similar in different viewing angles.

Figure 12 shows the stellar attenuation parameter $E(B-V)_{\rm star}$ as a function of b/a and $\log_{10}t_L$ for the DIG and H II regions. The two types of regions behave similarly, with $E(B-V)_{\rm star}$ decreasing as both b/a and $\log_{10}t_L$ increase. For DIG regions, the dependence of $E(B-V)_{\rm star}$ on b/a appears to be contradictory to the independence of $E(B-V)_{\rm gas}$ on b/a. The stronger stellar attenuation at smaller b/a indicates that the nonionizing continuum photons emitted from stars must have propagated a longer path than the ionizing photons emerging in the outskirt of the galaxy. The ionized gas regions are selected from the two-dimensional map of $\Sigma_{\rm H\alpha}$, and so they include emission and attenuation along the line of sight. Therefore the stellar continuum of each DIG region is not emitted from the DIG region itself, but is the integration of the attenuated continuum photons from all stars in the area covered by the region in question, while the ionizing photons are produced in the DIG region. This conjecture is supported by the similar behaviors of DIG and H II regions in the right-hand panel of Figure 12, which again shows the driving role of the stellar age in the stellar attenuation.

4.3. The Dominant Role of Stellar Age, and the Dust Model of Charlot & Fall (2000)

We find in this paper that the stellar age plays the dominant role in driving the correlation of stellar dust attenuation with many other regional/global properties of galaxies (see Section 3.1). As a result, the stellar age together with $\Sigma_{\rm H\alpha}$ can explain the properties of $E(B-V)_{\rm star}/E(B-V)_{\rm gas}$ in both H II and DIG regions (see Section 3.4). Of all the correlations we considered, the strongest is found between $E(B-V)_{\rm star}/E(B-V)_{\rm gas}$ and $\log_{10}t_L$ with a Spearman rank correlation coefficient $\rho=-0.63$ (Figure 3). The stellar attenuation itself has a strong correlation also with the stellar age, with $\rho=-0.569$ for the $E(B-V)_{\rm star}$–$\log_{10}t_L$ relation (Figure 3). The negative correlation of $E(B-V)_{\rm star}$ with stellar age is expected because stars are born in environments with enhanced dust contents (Panuzzo et al. 2007). Such an age-dependent stellar attenuation has been considered in some earlier studies (e.g., Noll et al. 2009; Buat et al. 2012; Lo Faro et al. 2017; Tress et al. 2019).

In DIG regions, the ionizing source is distributed in the outskirts of galaxies, while the stellar continuum is dominated by the underlying stars of intermediate/old ages in the ISM (see Section 4.2). Consequently, ionizing photons are less affected by the attenuation than nonionizing continuum photons. The strong correlation between $E(B-V)_{\rm star}/E(B-V)_{\rm gas}$ and $\log_{10}t_L$ actually reveals the expected correlation between $E(B-V)_{\rm star}$ and $\log_{10}t_L$ in DIG regions.

In H II regions, our results are broadly consistent with the dust model of Charlot & Fall (2000). In this model, nonionizing continuum photons emitted by young stars and ionizing photons propagate through both the HI envelope of the birth clouds, where young stars are born and embedded, before propagating through the ambient ISM, while emission from long-lived (old) stars only propagates through the ISM because of the finite lifetime of the stellar birth clouds. As emphasized in Charlot & Fall (2000), the finite lifetime of birth clouds is a key ingredient for resolving the discrepancy between the attenuation of line and continuum photons. In very young H II regions, most of the stars are still embedded in birth clouds, so that the stellar attenuation is comparable to the gas attenuation. Basu-Zych et al. (2007) studied a sample of ultraviolet-luminous galaxies whose $E(B-V)_{\rm star}$ are comparable to $E(B-V)_{\rm gas}$. They found that galaxies whose stars formed only recently are very young and can be explained by a model in which the majority of stars are within birth clouds. In very old H II regions, in which the stellar continuum is dominated by old stars in the ISM, both $E(B-V)_{\rm star}$ and $E(B-V)_{\rm star}/E(B-V)_{\rm gas}$ are low, as seen in Figure 3. The intermediate-age H II regions may be considered as a mixture of both young H II regions and old H II regions, so that their $E(B-V)_{\rm star}/E(B-V)_{\rm gas}$ cover the whole range from zero to unity. This is supported by the results shown in Figure 8, where younger H II regions tend to have a steeper slope, and almost all the regions are below the 1:1 relation at $\log_{10}\Sigma_{\rm H\alpha} > 39.5$.

4.4. Feature Importance of the Properties Based on Machine Learning

In Section 3.1 we have examined the correlation of dust attenuations with a large number of regional/global properties. The relative importance of different properties is quantified by the commonly used Spearman rank correlation coefficient. The technique of machine learning is widely applied today to more efficiently deal with these big-data problems. Here we also performed a machine-learning analysis as a consistency check on our results. We use `LightGBM`,[11] which is a gradient boosting framework using tree-based learning algorithms to evaluate the feature importance of the regional/global properties of our galaxies to the dust attenuation parameters.

Figure 13 shows the feature importance of all the 16 properties for $E(B-V)_{\rm star}$, $E(B-V)_{\rm gas}$, $E(B-V)_{\rm gas}-E(B-V)_{\rm star}$, and $E(B-V)_{\rm star}/E(B-V)_{\rm gas}$, respectively. Overall, it is encouraging that the results are well consistent with our previous analysis based on Spearman correlation coefficients: stellar age is indeed the most important property

[11] https://lightgbm.readthedocs.io/en/latest/index.html

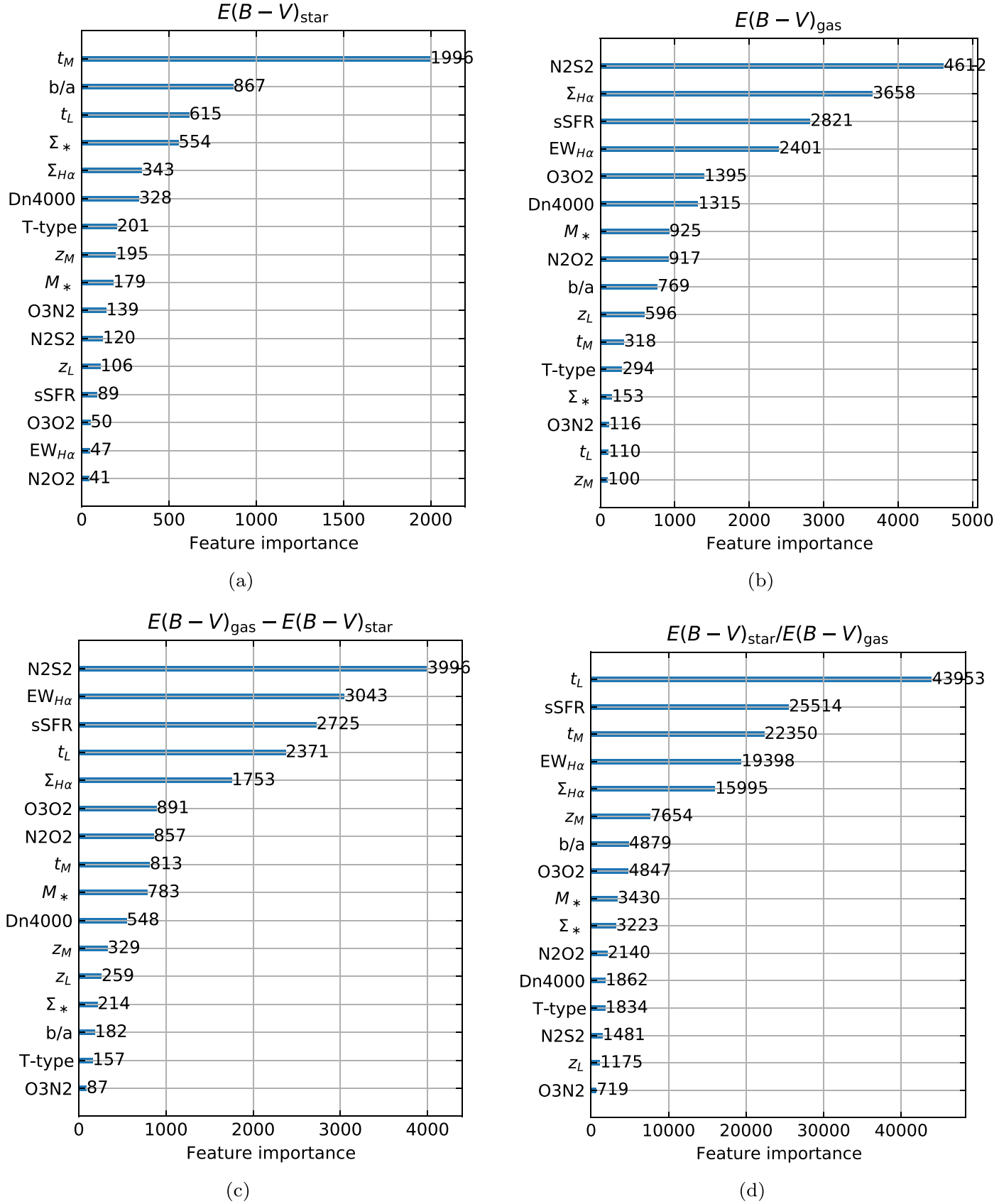

Figure 13. Feature importance of the 16 regional/global properties is shown for the four dust attenuation parameters (panels (a)–(d)): $E(B-V)_{\rm star}$, $E(B-V)_{\rm gas}$, $E(B-V)_{\rm gas}-E(B-V)_{\rm star}$, and $E(B-V)_{\rm star}/E(B-V)_{\rm gas}$. N2S2, N2O2, and O3O2 represent [N II]/[S II], [N II]/[O II], and [O III]/[O II].

for $E(B-V)_{\rm star}$ and $E(B-V)_{\rm star}/E(B-V)_{\rm gas}$, and [N II]/[S II] and $\Sigma_{\rm H\alpha}$ are the most important properties for $E(B-V)_{\rm gas}$. In particular, the mass-weighted age (t_M) shows the highest feature importance for $E(B-V)_{\rm star}$, while the luminosity-weighted age (t_L) is most important for $E(B-V)_{\rm star}/E(B-V)_{\rm gas}$. This is also in good agreement with the Spearman correlation analysis, where $E(B-V)_{\rm star}$ has a correlation coefficient of $\rho=-0.627$ with t_M (Appendix A) and $\rho=-0.529$ with t_L (Figure 3), and the strongest correlation is found between $E(B-V)_{\rm star}/E(B-V)_{\rm gas}$ and t_L with $\rho=-0.631$ (Figure 3). It is interesting to note that the b/a shows a high feature importance for $E(B-V)_{\rm star}$, falling in between t_M and t_L in panel (a) of the figure. The Spearman correlation coefficient between $E(B-V)_{\rm star}$ and b/a is relatively low ($\rho=-0.228$; Appendix A), however. This is probably because b/a is a global parameter, thus more sensitive to the overall stellar dust attenuation of the whole galaxy, while the Spearman correlation coefficients simply reflect the average behavior of individual regions. In this regard, the machine learning appears to be more powerful in comprehensively revealing the intrinsic correlations in a complex, high-dimensional data set.

5. Summary

In this paper, we study the relationship between $E(B-V)_{\rm star}$ and $E(B-V)_{\rm gas}$ in both H II regions and DIG regions of kiloparsec scales using data of integral field spectroscopy from the MaNGA MPL-9. For each region, we stack the original spectra and perform a full spectral fitting to obtain $E(B-V)_{\rm star}$ and other properties of the underlying stellar populations. We then measure emission lines from the starlight-subtracted spectra and calculate $E(B-V)_{\rm gas}$ from the Balmer decrement. With these measurements, we examine the correlations of $E(B-V)_{\rm star}$, $E(B-V)_{\rm gas}$, $E(B-V)_{\rm gas}-E(B-V)_{\rm star}$, and $E(B-V)_{\rm star}/E(B-V)_{\rm gas}$ with 16 regional/global properties. Our main results can be summarized as follows:

1. The relation between $E(B-V)_{\rm star}$ and $E(B-V)_{\rm gas}$ is stronger for more active H II regions.
2. Stellar age is the driving factor for $E(B-V)_{\rm star}$, and consequently for $E(B-V)_{\rm gas}-E(B-V)_{\rm star}$ and $E(B-V)_{\rm star}/E(B-V)_{\rm gas}$ as well. At fixed $\Sigma_{\rm H\alpha}$, the stellar age is linearly and negatively correlated with $E(B-V)_{\rm star}/E(B-V)_{\rm gas}$ at all ages.
3. Gas-phase metallicity and ionization level are important for $E(B-V)_{\rm gas}$.
4. The ionizing sources for DIG regions are likely distributed in the galaxy outskirts.
5. The attenuation in H II regions can be well explained by the two-component dust model of Charlot & Fall (2000).

We are grateful to the anonymous referee, whose comments have helped improve the paper. This work is supported by the National Key R&D Program of China (grant No. 2018YFA0404502), and the National Science Foundation of China (grant Nos. 11821303, 11973030, 11733004). M.B. acknowledges FONDECYT regular grant 1170618. M.G. acknowledges the funding from the STFC in the UK. R.R. acknowledges the Brazilian funding agencies CNPq, CAPES, and FAPERS.

Funding for the Sloan Digital Sky Survey IV has been provided by the Alfred P. Sloan Foundation, the U.S. Department of Energy Office of Science, and the Participating Institutions. SDSS-IV acknowledges support and resources from the Center for High-Performance Computing at the University of Utah. The SDSS website is www.sdss.org.

SDSS-IV is managed by the Astrophysical Research Consortium for the Participating Institutions of the SDSS Collaboration including the Brazilian Participation Group, the Carnegie Institution for Science, Carnegie Mellon University, the Chilean Participation Group, the French Participation Group, Harvard-Smithsonian Center for Astrophysics, Instituto de Astrofísica de Canarias, The Johns Hopkins University, Kavli Institute for the Physics and Mathematics of the Universe (IPMU)/University of Tokyo, Lawrence Berkeley National Laboratory, Leibniz Institut für Astrophysik Potsdam (AIP), Max-Planck-Institut für Astronomie (MPIA Heidelberg), Max-Planck-Institut für Astrophysik (MPA Garching), Max-Planck-Institut für Extraterrestrische Physik (MPE), National Astronomical Observatories of China, New Mexico State University,New York University, University of Notre Dame, Observatário Nacional/MCTI, The Ohio State University, Pennsylvania State University, Shanghai Astronomical Observatory, United Kingdom Participation Group, Universidad Nacional Autónoma de México, University of Arizona, University of Colorado Boulder, University of Oxford, University of Portsmouth, University of Utah, University of Virginia, University of Washington, University of Wisconsin, Vanderbilt University, and Yale University.

Appendix A
Correlations of Dust Attenuation Parameters with Regional/Global Properties

In the paper we have examined the correlation of dust attenuation with 13 regional properties and three global properties. Among other properties, $\log_{10}t_L$, $\Sigma_{\rm H\alpha}$, and [N II]/[S II] are found to be mostly correlated with the dust attenuation parameters, as shown in Figure 3 and discussed in detail in Section 3.1. Here we present the results for the remaining 13 properties. Following the format of Figure 3, Figure 14 shows the distribution of each property in the diagram of $E(B-V)_{\rm star}$ versus $E(B-V)_{\rm gas}$, as well as the correlation of the dust attenuation parameters with the properties. The Spearman rank correlation coefficient is indicated in each panel for both the full sample and the subset of H II regions as selected by $\log_{10}\Sigma_{\rm H\alpha}>39$. This figure, together with Figure 3, is discussed in depth in the paper. In what follows, we briefly mention several interesting points that can be obtained from the figure.

A dichotomy is present in the relation between the attenuation and Σ_* in the sense that the ionized gas regions can be divided into two classes separated at $\log_{10}\Sigma_*\sim 8$. This can be seen, for instance, in the top right panel where $E(B-V)_{\rm star}/E(B-V)_{\rm gas}$ decreases rapidly at $\log_{10}\Sigma_*<8$ and levels off at $\sim$0.5 when $\log_{10}\Sigma_*$ exceeds $\sim$8, a behavior very similar to the dichotomy in the relation between the attenuations and $\Sigma_{\rm H\alpha}$ as seen in the middle right panel of Figure 3. This similarity may be understood from the main sequence of star-forming regions of galaxies, in which the SFR is strongly correlated with stellar mass (e.g., Noeske et al. 2007; Peng et al. 2010; Whitaker et al. 2012; Cano-Díaz et al. 2016; Hsieh et al. 2017).

Our result reveals a positive correlation between $E(B-V)_{\rm star}/E(B-V)_{\rm gas}$ and sSFR, with $\rho=0.274$ (the last panel in the third row). This is consistent with many previous studies based on integrated spectra of galaxies (e.g., Wild et al. 2011; Price et al. 2014; Koyama et al. 2019; Qin et al. 2019), but it is different from that of Lin & Kong (2020), who found

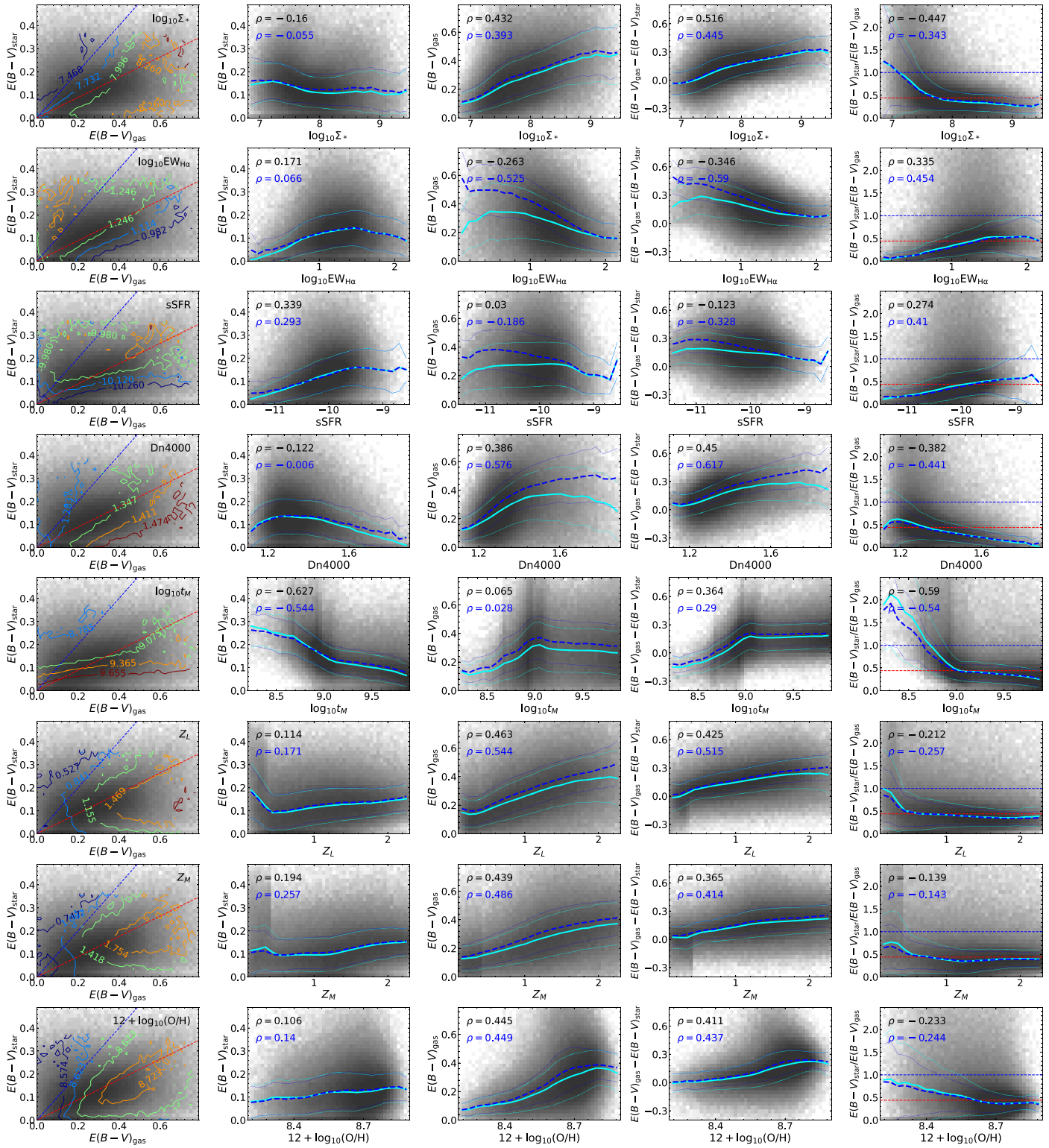

Figure 14. Correlations of $E(B-V)_{\rm star}$ and $E(B-V)_{\rm gas}$ to regional/global properties (panels from top to bottom): $\log_{10}\Sigma_*$, $\log_{10}{\rm EW}_{\rm H\alpha}$, sSFR, D_n4000, $\log_{10}t_M$, Z_L, Z_M, 12+$\log_{10}$(O/H), $\log_{10}$([N II]/[O II]), $\log_{10}$([O III]/[O II]), $\log_{10}M_*$, T-type, and b/a. Symbols and lines are the same as in Figure 3.

a negative correlation with $\rho\sim-0.24$. In our case, the attenuation parameters depend on ${\rm EW}_{\rm H\alpha}$ and sSFR in a similar way, which is expected as the ${\rm EW}_{\rm H\alpha}$ quantifies the strength of the Hα luminosity (essentially the SFR) relative to the stellar continuum luminosity (roughly proportional to Σ_*). For regions with $\log_{10}{\rm EW}_{\rm H\alpha}\gtrsim1$ or sSFR $\gtrsim-10$, $E(B-V)_{\rm gas}-E(B-V)_{\rm star}$ is roughly constant at around zero and $E(B-V)_{\rm star}/E(B-V)_{\rm gas}$ is close to the value of 0.44, with a weak dependence on ${\rm EW}_{\rm H\alpha}$ or sSFR. At lower ${\rm EW}_{\rm H\alpha}$ and sSFR, both attenuation parameters are positively correlated with the two properties, with $E(B-V)_{\rm gas}-E(B-V)_{\rm star}>0$ and $E(B-V)_{\rm star}/E(B-V)_{\rm gas}<0.44$.

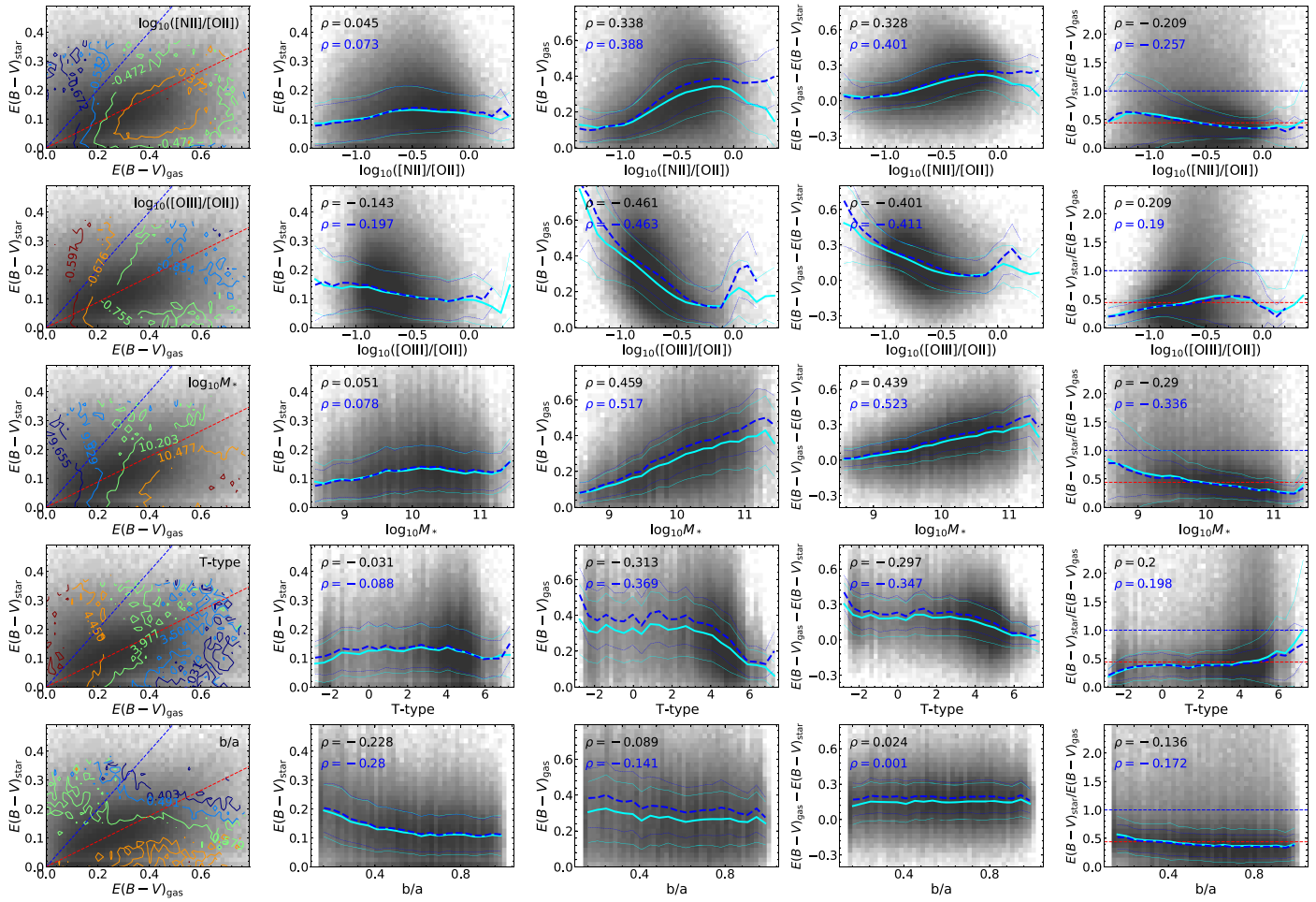

Figure 14. (Continued.)

Overall, all the dust attenuation parameters are weakly correlated with stellar metallicity, except in the most metal-poor regions, which appear to have higher $E(B-V)_{\rm star}$ and $E(B-V)_{\rm star}/E(B-V)_{\rm gas}$. The age t_M shows similar behaviors to t_L in its correlations with the attenuation parameters, but the correlation is much weaker for $t_M \gtrsim 1$ Gyr. The absence of a strong correlation at $t_M \gtrsim 1$ Gyr is particularly remarkable for $E(B-V)_{\rm gas}$. This result may be understood from the fact that t_M is dominated by low-mass old stars that contribute little to dust-related processes. As an empirical indicator of mean stellar age, the 4000 Å break is also correlated with the attenuation parameters, as expected. Similar to t_M, D_n4000 shows no correlation with $E(B-V)_{\rm gas}$ in old regions with $D_n4000 \gtrsim 1.5$, which may be explained by the known fact that D_n4000 is sensitive only to stellar populations younger than 1–2 Gyr (e.g., Kauffmann et al. 2003b).

The gas-phase metallicity $12+\log_{10}$(O/H) is estimated with the O3N2 estimator. The line ratio of [N II]/[O II] has also been frequently used to estimate the gas-phase metallicity, particularly when contribution from DIG becomes important (Zhang et al. 2017). Both parameters show a weak correlation with $E(B-V)_{\rm star}$, a positive correlation with $E(B-V)_{\rm gas}$ and $E(B-V)_{\rm gas}-E(B-V)_{\rm star}$, and a negative correlation with $E(B-V)_{\rm star}/E(B-V)_{\rm gas}$. The behaviors of $12+\log_{10}$(O/H) are quite similar to [N II]/[S II], but with weaker correlations with all the dust attenuation parameters. The ionization parameter [O III]/[O II] correlates with all the dust attenuation parameters, but in a different way from the metallicity parameters. These trends are broadly consistent with Lin & Kong (2020, see their Figure 8).

Figure 14 also shows the correlations of the dust attenuation parameters of ionized gas regions with three global properties of their host galaxies: M_*, T-type, and b/a. The $E(B-V)_{\rm star}$ shows no obvious correlation with $\log_{10}M_*$ and T-type, but decreases slightly with increasing b/a. The latter result is understandable. Smaller b/a corresponds to more inclined disks where starlight has to travel through the dusty ISM with a longer path. The $E(B-V)_{\rm gas}$ increases with stellar mass and shows anticorrelations with T-type and b/a. The $E(B-V)_{\rm gas}-E(B-V)_{\rm star}$ shows a slightly positive correlation with $\log_{10}M_*$, a slightly negative correlation with T-type, and a weak or no correlation with b/a. The $E(B-V)_{\rm star}/E(B-V)_{\rm gas}$ decreases with stellar mass. This result is consistent with that in Lin & Kong (2020), who found that the globally averaged $E(B-V)_{\rm star}/E(B-V)_{\rm gas}$ is a linearly decreasing function of $\log_{10}M_*$ (see their Figure 10). The $E(B-V)_{\rm star}/E(B-V)_{\rm gas}$ shows a slightly positive correlation with T-type and almost no correlation with b/a. Generally, the trends of the dust attenuation parameters with the global properties are consistent with the correlations with the regional properties, as described above.

Appendix B
Role of Specific Properties in Driving Dust Attenuation

Section 3.2 examines the role of stellar age in driving stellar attenuation, and Section 3.3 investigates the role of $\Sigma_{\rm H\alpha}$, [N II]/[S II] and [O III]/[O II] in driving the attenuation in gas. In these sections, for simplicity, results are shown only for some of the dust attenuation parameters or regional/global properties. Here we present the remaining results for completeness.

Figures 15 and 16 show the correlations of the two dust attenuation parameters, $E(B-V)_{\rm gas}-E(B-V)_{\rm star}$ and $E(B-V)_{\rm star}/E(B-V)_{\rm gas}$, respectively, with all the regional/global properties, aiming to test the dominant role of $\log_{10}t_L$. These figures follow the same format as Figure 4 and provide

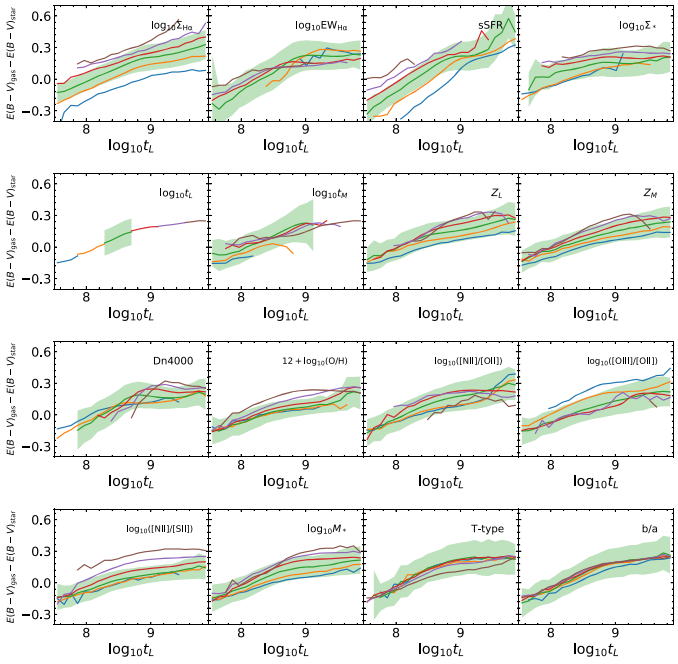

(a) $E(B-V)_{\rm gas}-E(B-V)_{\rm star}$ versus $\log_{10}t_L$

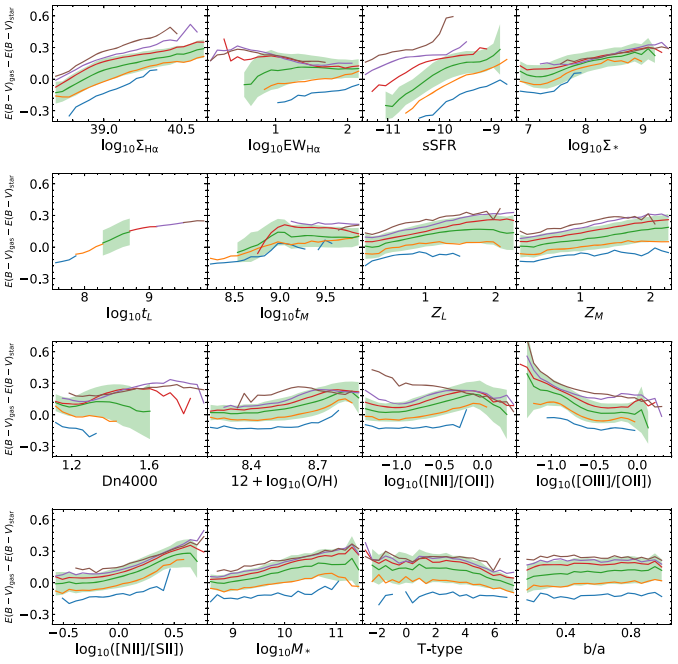

(b) $E(B-V)_{\rm gas}-E(B-V)_{\rm star}$ versus regional/global properties

Figure 15. $E(B-V)_{\rm gas}-E(B-V)_{\rm star}$ as function of stellar age ($\log_{10}t_L$) for ionized gas regions in different intervals of regional/global properties (panels (a)), and as functions of regional/global properties, but in different intervals of $\log_{10}t_L$ (panels (b)). Symbols and lines are the same as in Figure 4.

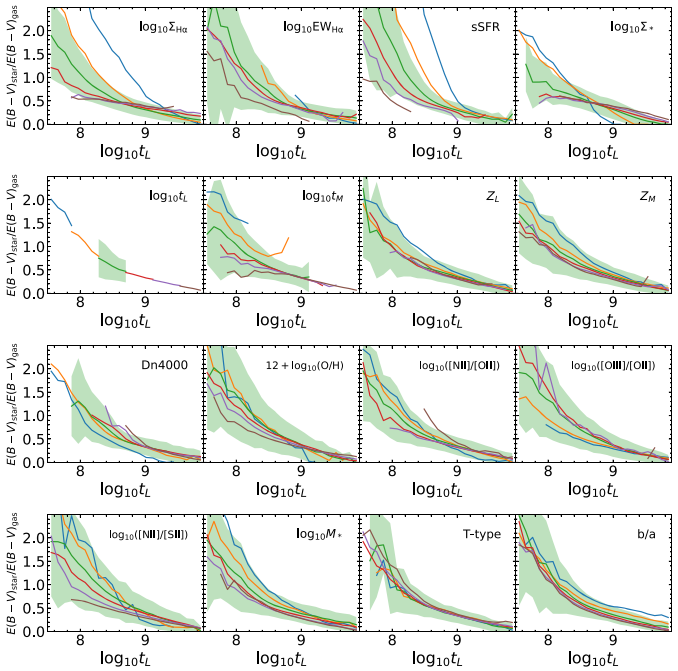

(a) $E(B-V)_{\rm star}/E(B-V)_{\rm gas}$ versus $\log_{10}t_L$

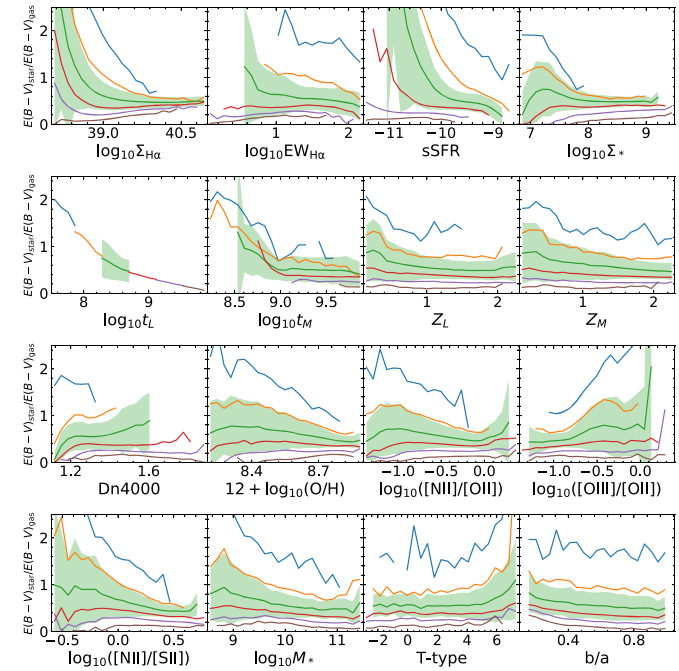

(b) $E(B-V)_{\rm star}/E(B-V)_{\rm gas}$ versus regional/global properties

Figure 16. $E(B-V)_{\rm star}/E(B-V)_{\rm gas}$ as functions of stellar age ($\log_{10}t_L$), but in different intervals of regional/global properties (panels (a)), and as function of regional/global properties, but in different intervals of $\log_{10}t_L$ (panels (b)). Symbols and lines are the same as in Figure 4.

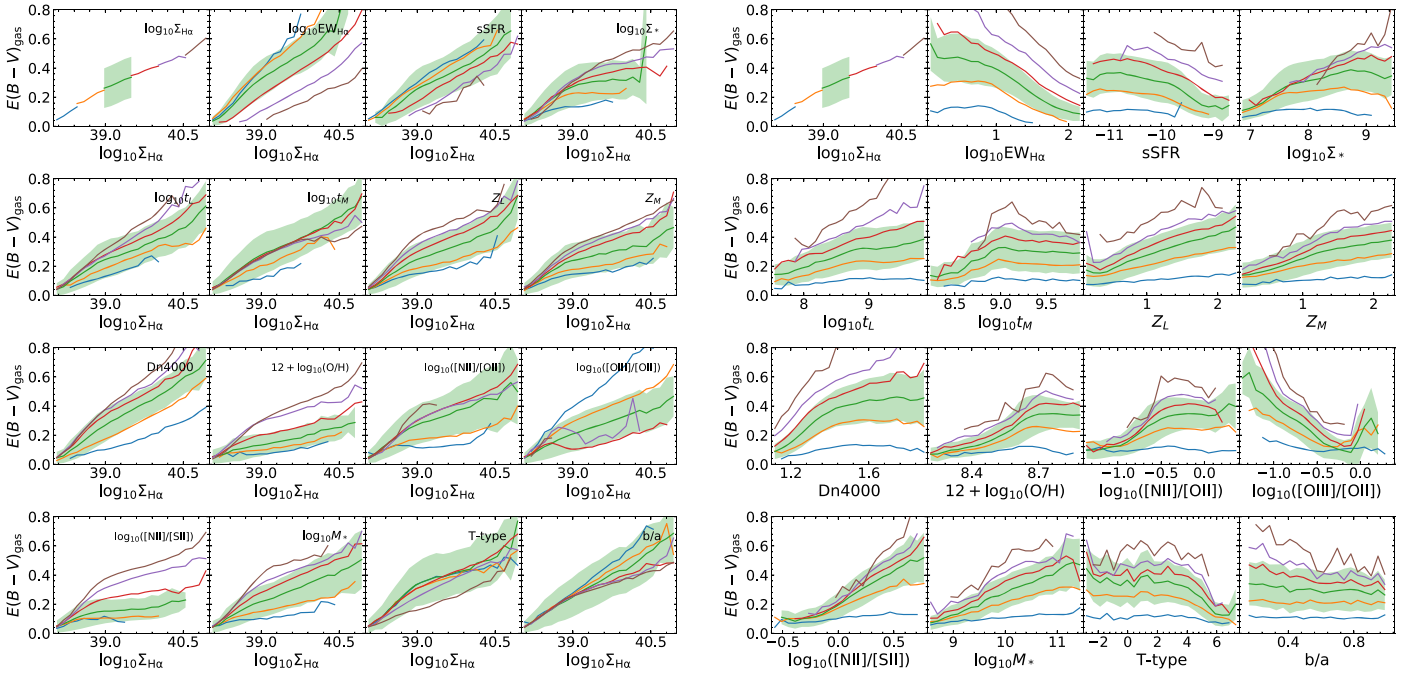

(a) $E(B-V)_{\rm gas}$ versus $\log_{10}\Sigma_{\rm H\alpha}$ (b) $E(B-V)_{\rm gas}$ versus regional/global properties

Figure 17. $E(B-V)_{\rm gas}$ as functions of $\Sigma_{\rm H\alpha}$, but in different intervals of regional/global properties (panels (a)), and as function of regional/global properties, but in different intervals of $\Sigma_{\rm H\alpha}$ (panels (b)). Symbols and lines are the same as in Figure 4.

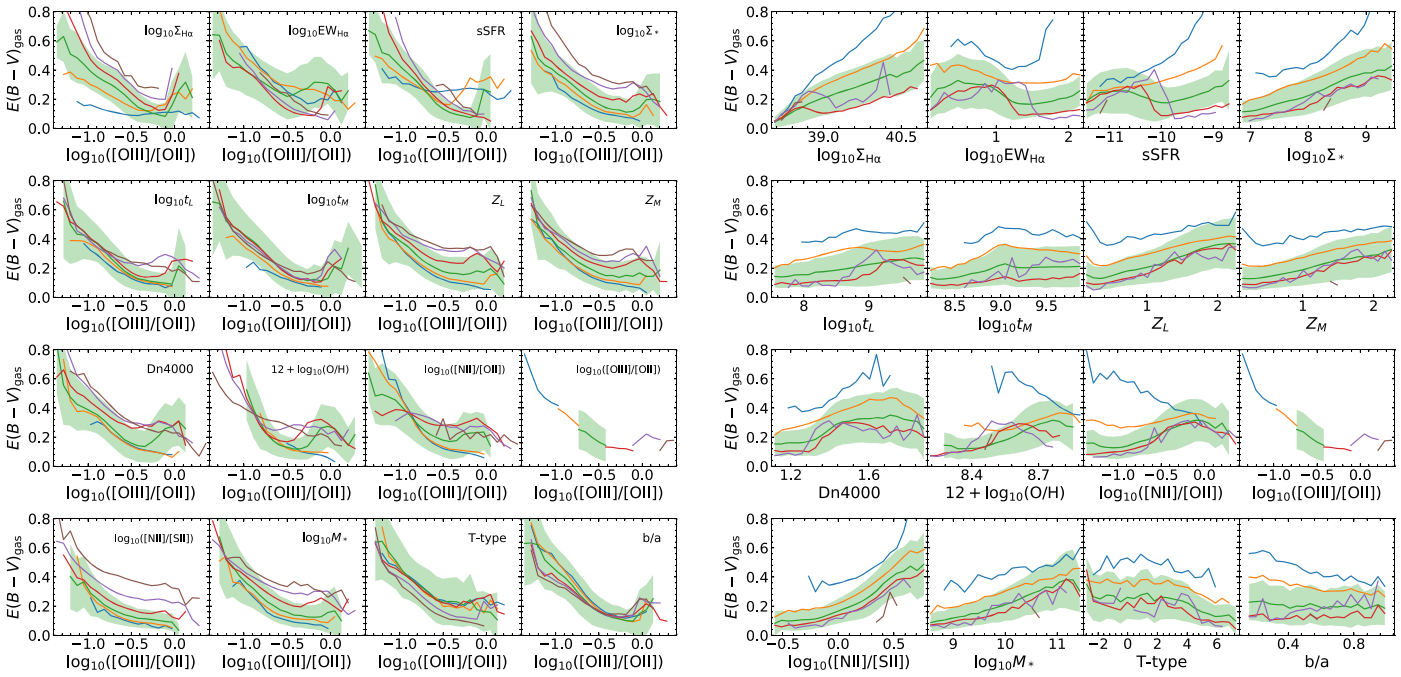

(a) $E(B-V)_{\rm gas}$ versus $\log_{10}$[O III]/[O II] (b) $E(B-V)_{\rm gas}$ versus regional/global properties

Figure 18. $E(B-V)_{\rm gas}$ as functions of [O III]/[O II], but in different intervals of regional/global properties (panels (a)), and as function of regional/global properties, but in different intervals of [O III]/[O II] (panels (b)). Symbols and lines are the same as in Figure 4.

complementary results to the analysis in Section 3.2. Each figure contains two sets of panels. In panel set (a), the dust attenuation parameter is plotted as function of $\log_{10}t_L$, but for different subsets of the ionized gas regions selected by different regional/global properties. In panel set (b), the full sample is divided into subsets according to $\log_{10}t_L$, and the dust attenuation parameter of each subset is plotted as function of the different regional/global properties. Figure 4 shows that stellar age is indeed a driving property for the stellar attenuation. The two figures here further show that the stellar age also plays an important role in driving the difference and ratio of the stellar and gas attenuation. This result is produced

by the combined effect of the strong correlation of $\log_{10}t_L$ with $E(B-V)_{\rm star}$ and the moderate correlation of $\log_{10}t_L$ with $E(B-V)_{\rm gas}$, as discussed in Sections 3.2 and 3.3.

Figures 17 and 18 examine the correlation of $E(B-V)_{\rm gas}$ with the 16 regional/global properties, aiming to test the importance of $\Sigma_{\rm H\alpha}$ and [O III]/[O II] in driving the attenuation in gas. These figures follow the same format as Figure 5, which tests the role of [N II]/[S II], and they provide complementary results to the analysis in Section 3.3. Each figure contains two sets of panels, with one plotting $E(B-V)_{\rm gas}$ as a function of either $\Sigma_{\rm H\alpha}$ or [O III]/[O II] for subsets of ionized gas regions selected by different properties, and the other plotting $E(B-V)_{\rm gas}$ as a function of different properties for subsets of ionized gas regions selected by either $\Sigma_{\rm H\alpha}$ or [O III]/[O II]. Comparing the two figures here with Figure 5, one can find that [N II]/[S II] shows a stronger correlation with the gas attenuation than $\Sigma_{\rm H\alpha}$ and [O III]/[O II].

ORCID iDs

Niu Li https://orcid.org/0000-0002-0656-075X
Cheng Li https://orcid.org/0000-0002-8711-8970
Shuang Zhou https://orcid.org/0000-0002-8999-6814
Fu-heng Liang https://orcid.org/0000-0003-2496-1247
Niv Drory https://orcid.org/0000-0002-7339-3170
Rogério Riffel https://orcid.org/0000-0002-1321-1320

References

Aguado, D. S., Ahumada, R., Almeida, A., et al. 2019, ApJS, 240, 23
Alloin, D., Collin-Souffrin, S., Joly, M., & Vigroux, L. 1979, A&A, 78, 200
Anderson, L. D., Wenger, T. V., Armentrout, W. P., Balser, D. S., & Bania, T. M. 2019, ApJ, 871, 145
Aoyama, S., Hou, K.-C., Shimizu, I., et al. 2017, MNRAS, 466, 105
Asari, N. V., Cid Fernandes, R., Stasińska, G., et al. 2007, MNRAS, 381, 263
Baldwin, J. A., Phillips, M. M., & Terlevich, R. 1981, PASP, 93, 5
Balogh, M. L., Morris, S. L., Yee, H. K. C., Carlberg, R. G., & Ellingson, E. 1999, ApJ, 527, 54
Barnes, J. E., Wood, K., Hill, A. S., & Haffner, L. M. 2014, MNRAS, 440, 3027
Barnes, J. E., Wood, K., Hill, A. S., & Haffner, L. M. 2015, MNRAS, 447, 559
Basu-Zych, A. R., Schiminovich, D., Johnson, B. D., et al. 2007, ApJS, 173, 457
Battisti, A. J., Calzetti, D., & Chary, R.-R. 2017a, ApJ, 840, 109
Battisti, A. J., Calzetti, D., & Chary, R.-R. 2017b, ApJ, 851, 90
Bertelli, G., Bressan, A., Chiosi, C., Fagotto, F., & Nasi, E. 1994, A&AS, 106, 275
Bianchi, S., & Ferrara, A. 2005, MNRAS, 358, 379
Blanton, M. R., Bershady, M. A., Abolfathi, B., et al. 2017, AJ, 154, 28
Blanton, M. R., Kazin, E., Muna, D., Weaver, B. A., & Price-Whelan, A. 2011, AJ, 142, 31
Blanton, M. R., Schlegel, D. J., Strauss, M. A., et al. 2005, AJ, 129, 2562
Blitz, L., & Shu, F. H. 1980, ApJ, 238, 148
Boquien, M., Burgarella, D., Roehlly, Y., et al. 2019, A&A, 622, A103
Bruzual, G., & Charlot, S. 2003, MNRAS, 344, 1000
Buat, V., Boquien, M., Małek, K., et al. 2018, A&A, 619, A135
Buat, V., Noll, S., Burgarella, D., et al. 2012, A&A, 545, A141
Bundy, K., Bershady, M. A., Law, D. R., et al. 2015, ApJ, 798, 7
Calzetti, D., Armus, L., Bohlin, R. C., et al. 2000, ApJ, 533, 682
Calzetti, D., Kinney, A. L., & Storchi-Bergmann, T. 1994, ApJ, 429, 582
Cano-Díaz, M., Sánchez, S. F., Zibetti, S., et al. 2016, ApJL, 821, L26
Cardelli, J. A., Clayton, G. C., & Mathis, J. S. 1989, ApJ, 345, 245
Chabrier, G. 2003, PASP, 115, 763
Charlot, S., & Fall, S. M. 2000, ApJ, 539, 718
Chevallard, J., Charlot, S., Wandelt, B., & Wild, V. 2013, MNRAS, 432, 2061
Cid Fernandes, R. 2018, MNRAS, 480, 4480
Cid Fernandes, R., Mateus, A., Sodré, L., Stasińska, G., & Gomes, J. M. 2005, MNRAS, 358, 363
Cid Fernandes, R., Pérez, E., García Benito, R., et al. 2013, A&A, 557, A86
Conroy, C. 2013, ARA&A, 51, 393
Croom, S. M., Lawrence, J. S., Bland-Hawthorn, J., et al. 2012, MNRAS, 421, 872
Denicoló, G., Terlevich, R., & Terlevich, E. 2002, MNRAS, 330, 69
Domínguez Sánchez, H., Huertas-Company, M., Bernardi, M., Tuccillo, D., & Fischer, J. L. 2018, MNRAS, 476, 3661
Dominik, C., & Tielens, A. G. G. M. 1997, ApJ, 480, 647
Dopita, M. A., Sutherland, R. S., Nicholls, D. C., Kewley, L. J., & Vogt, F. P. A. 2013, ApJS, 208, 10
Drory, N., MacDonald, N., Bershady, M. A., et al. 2015, AJ, 149, 77
Dwek, E. 1998, ApJ, 501, 643
Fanelli, M. N., O'Connell, R. W., & Thuan, T. X. 1988, ApJ, 334, 665
Fitzpatrick, E. L. 1999, PASP, 111, 63
Galliano, F., Galametz, M., & Jones, A. P. 2018, ARA&A, 56, 673
Ge, J., Yan, R., Cappellari, M., et al. 2018, MNRAS, 478, 2633
González Delgado, R. M., Cerviño, M., Martins, L. P., Leitherer, C., & Hauschildt, P. H. 2005, MNRAS, 357, 945
Gordon, K. D., Clayton, G. C., Misselt, K. A., Landolt, A. U., & Wolff, M. J. 2003, ApJ, 594, 279
Gordon, K. D., Clayton, G. C., Witt, A. N., & Misselt, K. A. 2000, ApJ, 533, 236
Greener, M. J., Aragón-Salamanca, A., Merrifield, M. R., et al. 2020, MNRAS, 495, 2305
Gunn, J. E., Siegmund, W. A., Mannery, E. J., et al. 2006, AJ, 131, 2332
Haffner, L. M., Dettmar, R. J., Beckman, J. E., et al. 2009, RvMP, 81, 969
Hirashita, H., & Kuo, T.-M. 2011, MNRAS, 416, 1340
Hsieh, B. C., Lin, L., Lin, J. H., et al. 2017, ApJL, 851, L24
Hunt, L. K., & Hirashita, H. 2009, A&A, 507, 1327
Kashino, D., Silverman, J. D., Rodighiero, G., et al. 2013, ApJ, 777, L8
Kauffmann, G., Heckman, T. M., Tremonti, C., et al. 2003a, MNRAS, 346, 1055
Kauffmann, G., Heckman, T. M., White, S. D. M., et al. 2003b, MNRAS, 341, 33
Kennicutt, R. C. J. 1984, ApJ, 287, 116
Kennicutt, R. C. J. 1998, ARA&A, 36, 189
Kewley, L. J., Groves, B., Kauffmann, G., & Heckman, T. 2006, MNRAS, 372, 961
Kewley, L. J., Heisler, C. A., Dopita, M. A., & Lumsden, S. 2001, ApJS, 132, 37
Kim, K.-T., & Koo, B.-C. 2001, ApJ, 549, 979
Koyama, Y., Shimakawa, R., Yamamura, I., Kodama, T., & Hayashi, M. 2019, PASJ, 71, 8
Kreckel, K., Groves, B., Schinnerer, E., et al. 2013, ApJ, 771, 62
Lacerda, E. A. D., Cid Fernandes, R., Couto, G. S., et al. 2018, MNRAS, 474, 3727
Law, D. R., Cherinka, B., Yan, R., et al. 2016, AJ, 152, 83
Li, C., Wang, T.-G., Zhou, H.-Y., Dong, X.-B., & Cheng, F.-Z. 2005, AJ, 129, 669
Li, N., Li, C., Mo, H., et al. 2020, ApJ, 896, 38
Liang, F.-H., Li, C., Li, N., et al. 2020, ApJ, 896, 121
Lin, Z., & Kong, X. 2020, ApJ, 888, 88
Lo Faro, B., Buat, V., Roehlly, Y., et al. 2017, MNRAS, 472, 1372
Lopez, L. A., Krumholz, M. R., Bolatto, A. D., Prochaska, J. X., & Ramirez-Ruiz, E. 2011, ApJ, 731, 91
Masters, K. L., Krawczyk, C., Lintott, C., & Simmons, B. 2021, BAAS, 53, 1
Meurer, G. R., Heckman, T. M., & Calzetti, D. 1999, ApJ, 521, 64
Nanni, A., Bressan, A., Marigo, P., & Girardi, L. 2013, MNRAS, 434, 2390
Noeske, K. G., Weiner, B. J., Faber, S. M., et al. 2007, ApJL, 660, L43
Noll, S., Burgarella, D., Giovannoli, E., et al. 2009, A&A, 507, 1793
Nozawa, T., Kozasa, T., Habe, A., et al. 2007, ApJ, 666, 955
Osterbrock, D. E., & Ferland, G. J. 2006, Astrophysics of Gaseous Nebulae and Active Galactic Nuclei (2nd ed.; Sausalito, CA: Univ. Science Books)
Pannella, M., Elbaz, D., Daddi, E., et al. 2015, ApJ, 807, 141
Panuzzo, P., Granato, G. L., Buat, V., et al. 2007, MNRAS, 375, 640
Peng, Y.-j., Lilly, S. J., Kovač, K., et al. 2010, ApJ, 721, 193
Pettini, M., & Pagel, B. E. J. 2004, MNRAS, 348, L59
Pilyugin, L. S. 2001, A&A, 369, 594
Pilyugin, L. S., & Thuan, T. X. 2005, ApJ, 631, 231
Popping, G., Somerville, R. S., & Galametz, M. 2017, MNRAS, 471, 3152
Prevot, M. L., Lequeux, J., Maurice, E., Prevot, L., & Rocca-Volmerange, B. 1984, A&A, 132, 389
Price, S. H., Kriek, M., Brammer, G. B., et al. 2014, ApJ, 788, 86
Puglisi, A., Rodighiero, G., Franceschini, A., et al. 2016, A&A, 586, A83
Qin, J., Zheng, X. Z., Wuyts, S., Pan, Z., & Ren, J. 2019, ApJ, 886, 28
Reddy, N. A., Erb, D. K., Pettini, M., Steidel, C. C., & Shapley, A. E. 2010, ApJ, 712, 1070
Reddy, N. A., Kriek, M., Shapley, A. E., et al. 2015, ApJ, 806, 259

Reynolds, R. J., & Cox, D. P. 1992, ApJL, 400, L33
Riffel, R., Mallmann, N. D., Ilha, G. S., et al. 2021, MNRAS, 501, 4064
Riffel, R., Pastoriza, M. G., Rodríguez-Ardila, A., & Bonatto, C. 2009, MNRAS, 400, 273
Riffel, R., Pastoriza, M. G., Rodríguez-Ardila, A., & Maraston, C. 2008, MNRAS, 388, 803
Salim, S., & Narayanan, D. 2020, ARA&A, 58, 529
Sánchez, S. F., Avila-Reese, V., Hernandez-Toledo, H., et al. 2018, RMxAA, 54, 217
Sánchez, S. F., Kennicutt, R. C., Gil de Paz, A., et al. 2012a, A&A, 538, A8
Sánchez, S. F., Rosales-Ortega, F. F., Marino, R. A., et al. 2012b, A&A, 546, A2
Schneider, R., Valiante, R., Ventura, P., et al. 2014, MNRAS, 442, 1440
Smee, S. A., Gunn, J. E., Uomoto, A., et al. 2013, AJ, 146, 32
Tomičić, N., Kreckel, K., Groves, B., et al. 2017, ApJ, 844, 155
Tremonti, C. A., Heckman, T. M., Kauffmann, G., et al. 2004, ApJ, 613, 898
Tress, M., Ferreras, I., Pérez-González, P. G., et al. 2019, MNRAS, 488, 2301
Urrutia, T., Wisotzki, L., Kerutt, J., et al. 2019, A&A, 624, A141
Valentino, F., Daddi, E., Strazzullo, V., et al. 2015, ApJ, 801, 132
Vazdekis, A., Koleva, M., Ricciardelli, E., Röck, B., & Falcón-Barroso, J. 2016, MNRAS, 463, 3409
Vazdekis, A., Sánchez-Blázquez, P., Falcón-Barroso, J., et al. 2010, MNRAS, 404, 1639
Wake, D. A., Bundy, K., Diamond-Stanic, A. M., et al. 2017, AJ, 154, 86
Westfall, K. B., Cappellari, M., Bershady, M. A., et al. 2019, AJ, 158, 231
Whitaker, K. E., van Dokkum, P. G., Brammer, G., & Franx, M. 2012, ApJL, 754, L29
Wild, V., Charlot, S., Brinchmann, J., et al. 2011, MNRAS, 417, 1760
Wilkinson, D. M., Maraston, C., Thomas, D., et al. 2015, MNRAS, 449, 328
Wuyts, S., Förster Schreiber, N. M., Lutz, D., et al. 2011, ApJ, 738, 106
Wuyts, S., Förster Schreiber, N. M., Nelson, E. J., et al. 2013, ApJ, 779, 135
Yan, R., & Blanton, M. R. 2012, ApJ, 747, 61
Yan, R., Bundy, K., Law, D. R., et al. 2016a, AJ, 152, 197
Yan, R., Tremonti, C., Bershady, M. A., et al. 2016b, AJ, 151, 8
Zahid, H. J., Kudritzki, R.-P., Conroy, C., Andrews, B., & Ho, I. T. 2017, ApJ, 847, 18
Zaritsky, D., Kennicutt, A. C. J., & Huchra, J. P. 1994, ApJ, 420, 87
Zhang, K., Yan, R., Bundy, K., et al. 2017, MNRAS, 466, 3217
Zhou, S., Mo, H. J., Li, C., et al. 2019, MNRAS, 485, 5256
Zhukovska, S. 2014, A&A, 562, A76